Thermoelectrics



The Thermoelectric Properties of Bismuth Telluride

Ian T. Witting, Thomas C. Chasapis, Francesco Ricci, Matthew Peters, Nicholas A. Heinz, Geoffroy Hautier, and G. Jeffrey Snyder*

Bismuth telluride is the working material for most Peltier cooling devices and thermoelectric generators. This is because Bi₂Te₃ (or more precisely its alloys with Sb₂Te₃ for p-type and Bi₂Se₃ for n-type material) has the highest thermoelectric figure of merit, zT, of any material around room temperature. Since thermoelectric technology will be greatly enhanced by improving Bi₂Te₃ or finding a superior material, this review aims to identify and quantify the key material properties that make Bi₂Te₃ such a good thermoelectric. The large zT can be traced to the high band degeneracy, low effective mass, high carrier mobility, and relatively low lattice thermal conductivity, which all contribute to its remarkably high thermoelectric quality factor. Using literature data augmented with newer results, these material parameters are quantified, giving clear insight into the tailoring of the electronic band structure of Bi₂Te₃ by alloying, or reducing thermal conductivity by nanostructuring. For example, this analysis clearly shows that the minority carrier excitation across the small bandgap significantly limits the thermoelectric performance of Bi₂Te₃, even at room temperature, showing that larger bandgap alloys are needed for higher temperature operation. Such effective material parameters can also be used for benchmarking future improvements in Bi₂Te₃ or new replacement materials.

1. Introduction

Bismuth telluride, Bi_2Te_3 and its alloys with Sb_2Te_3 and Bi_2Se_3 are the most important class of thermoelectric materials because they have the highest known efficiency near room temperature despite numerous attempts to discover better materials. Being the best material, virtually every Peltier cooler

I. T. Witting, Dr. T. C. Chasapis, Dr. M. Peters, Prof. G. J. Snyder Department of Materials Science and Engineering Northwestern University

2220 Campus Drive, Cook Hall 2036, Evanston, IL 60208, USA E-mail: jeff.snyder@northwestern.edu

Dr. F. Ricci, Prof. G. Hautier Institute of Condensed Matter and Nanosciences Université catholique de Louvain Louvain-la-Neuve 1348, Belgium Dr. N. A. Heinz

National Aeronautics and Space Administration Jet Propulsion Laboratory

4800 Oak Grove Drive, La Cañada Flintridge, CA 91011, USA

The ORCID identification number(s) for the author(s) of this article can be found under https://doi.org/10.1002/aelm.201800904.

DOI: 10.1002/aelm.201800904

made for efficient thermoelectric cooling or temperature management uses Bi₂Te₃ alloys. Such solid-state devices dominate the market for temperature control in optoelectronics. As the need to eliminate greenhouse-gas refrigerants increases, Peltier cooling is becoming more attractive particularly in small systems where efficiencies are comparable to traditional refrigerant based cooling. Such small devices may enable distributive heating/ cooling (only where and when it is needed) with higher system level energy efficiency, for example in electric vehicles where energy for heating/cooling competes with vehicle range. Even for thermoelectric power generation, e.g., recovery of waste heat, Bi₂Te₃ alloys are most used because of superior efficiency up to 200 °C and the technology to make devices with Bi₂Te₃ is most advanced.[1-3]

While the material and production technology for making Bi₂Te₃-based devices has remained essentially unchanged since the 1960s, our understanding of these materials has advanced considerably. Most

recently, the interest in topological insulators (TI) has led to new insights into the complex electronic structure^[4,5] revealing that with the accuracy in assessing the band structures available today, improvements in the electronic structure by band engineering should not only be possible but predictable.^[6–9] Indeed, the p-type alloys chosen for use in commercial Peltier coolers appear to have unintentionally arrived at a composition close to a band convergence. The understanding of defects and doping is also advancing rapidly that will lead to new strategies for additional improvements in the electronic properties.

The thermal conductivity of Bi_2Te_3 -based alloys can also be engineered, where in particular there is much recent interest in microstructure engineering or nanostructuring. [10–22] Reduced thermal conductivity has led to numerous reports of exceptionally high efficiency (zT) that would be sufficient to revolutionize the industry. However, between measurement and material uncertainties, a revolutionary new Bi_2Te_3 -based material has not made it to the market. Because even small but reliable improvements could make significant impact, it is worthwhile to better understand all the complex, interdependent effects of band engineering and microstructure engineering. To demonstrate and quantify improvements in thermoelectric properties, it is necessary to have well characterized properties or reliable benchmarks for comparison.



It is the goal of this review to provide benchmark properties of Bi₂Te₃ to serve as a basis of comparison when improving Bi₂Te₃ or finding a new material to replace it. While alloys containing bismuth telluride are the state-of-the-art, we intentionally focus primarily on the properties of the binary compound. By doing so, we aim to explain the fundamental properties making this material such an outstanding thermoelectric near room temperature, but also explore its weaknesses which necessitate alloying and further engineering. Other recent reviews have focused on the complex electronic structures and relationship to topological insulating behavior. Here, after a discussion of the atomic structure of Bi₂Te₃ as it relates to the complex electronic band structure beneficial to thermoelectrics, we discuss the dominant charged defects, which determine the electronic properties, and their relationship to synthesis and processing conditions. We then compile and analyze the most reliable thermoelectric data of oriented Bi₂Te₃ from past studies and reviews[1,11-13,44,45] to extract the effective material properties that can be altered by band and microstructure engineering.

2. Structure and Chemistry

2.1. Crystal Structure

Bismuth telluride Bi_2Te_3 , along with Sb_2Te_3 and Bi_2Se_3 , crystallizes in the tetradymite crystal structure shown in **Figure 1**. The coordination of Bi and Te is octahedral much like Pb and Te in the lead chalcogenide IV–VI semiconductors having the rock salt structure. The slightly less electronegative Bi compared to more electronegative Te justifies the association of valence as Bi^{+3} (s^2p^0) and Te^{-2} . Like rock salt PbTe, the large Te^{-2} anions of Bi_2Te_3 form a close-packed layer with cations (Bi^{+3} in Bi_2Te_3 or Pb^{+2} in PbTe) in octahedral holes. While rock salt PbTe has an FCC cubic packing of close-packed Te layers, Bi_2Te_3 has a hexagonal HCP arrangement of Te layers. Charge balance is maintained in the

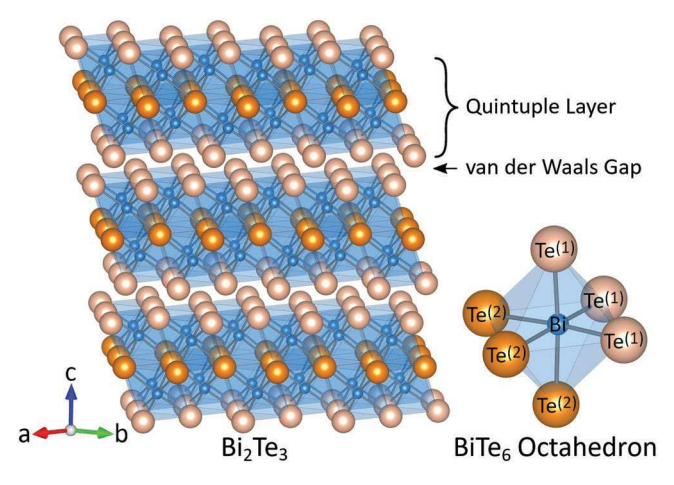


Figure 1. Layered structure of Bi_2Te_3 . Bismuth atoms are octahedrally coordinated by tellurium atoms residing on two inequivalent sites, distinguished here by tone and notation. Each quintuple layer lamella is separated by weak van der Waals bonding between adjacent $Te^{(1)}$ layers.



lan Witting earned his Master of Science in Materials Science and Engineering from North Carolina State University in 2008. He is currently a Ph.D. candidate in the Department of Materials Science and Engineering at Northwestern University under the direction of Dr. G. Jeffrey Snyder. His research interests include the

engineering of electronic properties and microstructure of thermoelectric materials, as well as single crystal growth of thermoelectrics.



Francesco Ricci obtained a Master's in Physics from the University of Cagliari (Italy), with a thesis about chaotic coupled systems. He received his Ph.D. in Physics from the University of Cagliari under the supervision of Vincenzo Fiorentini with research focused on multiferroic tunnel junctions, ferroelectric materials, and transparent

conducting oxides by using ab initio methods. He is currently a post-doctoral researcher at the Université catholique de Louvain. The topic of his current research concerns the use of high-throughput approaches for discovering new thermoelectric materials.



G. Jeffrey Snyder is a Professor of Materials Science and Engineering at Northwestern University in Evanston, Illinois. His interests are focused on materials physics and chemistry for thermoelectric engineering, such as band engineering, design of complex Zintl compounds, and use of nanostructured composites.

His interdisciplinary approach stems from studies of solid state chemistry at Cornell University and the Max Planck Institute for Solid State Research, applied physics at Stanford University, and thermoelectric materials and device engineering at NASA/Jet Propulsion Laboratory and California Institute of Technology (Caltech).

tetradymite V–VI semiconductors by the elimination of a metal layer every five close-packed planes to form a rhombohedral structure.^[23] These "quintuple" layers form in the

sequence $Te^{(1)}$ — Bi — $Te^{(2)}$ — Bi — $Te^{(1)}$, where the numbers contained in parenthesis distinguish the inequivalent Te sites. The Te — Bi bonds are polar-covalent while only weak van der Waals type bonding exists between the neighboring, $Te^{(1)}$ — $Te^{(1)}$ planes. Having large atoms with relatively weak bonds that are highly polarizable and relatively anharmonic has important consequences for the lattice thermal conductivity and the static dielectric constant. $I^{(4,24,25)}$

The layered structure of Bi₂Te₃ and the weakness of the Te⁽¹⁾ – Te⁽¹⁾ bonds between the quintuples are responsible for the easy cleavage along the basal planes (a and b directions) as well as mechanical^[26] and electrical anisotropy.^[5,27–32] The electrical conductivity within the basal planes is greater than that across the van der Waals gap (along the c axis) with the ratio as high as 6 in n-type and 3 in p-type Bi₂Te₃. [29,31,32] The lattice thermal conductivity along the basal planes is almost double that in the perpendicular direction.[31,32] As the anisotropy of the conductivity exceeds that of the thermal conductivity, single crystal and oriented polycrystals exhibit higher zT within the ab planes. The Seebeck coefficient, however, is nearly isotropic for both n- and p-type materials having extrinsic conduction as this largely originates from the isotropic density-of-states. It can become anisotropic when affected by bipolar conduction due to the difference in anisotropy of mobility between the conduction and valence bands.[28,33,34] In polycrystalline samples, the respective measured transport coefficients may be considered as effective averages of both the in- and out-ofplane directions.

2.2. Electronic Structure

Coupled with its inherently low lattice thermal conductivity. Bi₂Te₂ is an excellent thermoelectric because of its complex electronic band structure which has been explored extensively by experimental and theoretical studies. Although the semiconducting electronic structure of Bi₂Te₃ can be explained using simple valence rules, spin-orbit interactions complicate the band structure giving Bi₂Te₃ exceptional electronic properties.[35-46] The band structure of Bi₂Te₃ can be qualitatively understood by considering only the interactions of the valence p-states of both atoms within the quintuple layer.[37] The valence s and p levels in Bi and Te have significant enough separation that sp-hybridization is weak. The van der Waals interaction between the Te⁽¹⁾ atoms between neighboring quintuple layers are essentially nonbonding and contribute close to the top of the valence band while the Te-bonding states are generally lower in energy (Figure 2). The filled or lone pair Bi-s states of Bi+3 are further below in the valence band and do not contribute to the top of the valence band unlike the Pb⁺² s-states in lead chalcogenides.^[25] The conduction bands are comprised primarily of unfilled antibonding p-states of Bi used in bonding with Te. There are two bonding and two antibonding states between the Bi and Te atoms for each nonbonding state on the Te⁽¹⁾ atoms. The slightly polar nature of the bonding makes the Bi atoms somewhat positively charged while the Te atoms are negatively charged with the Te⁽¹⁾ atoms more negative than the $Te^{(2)}$.[37,47]

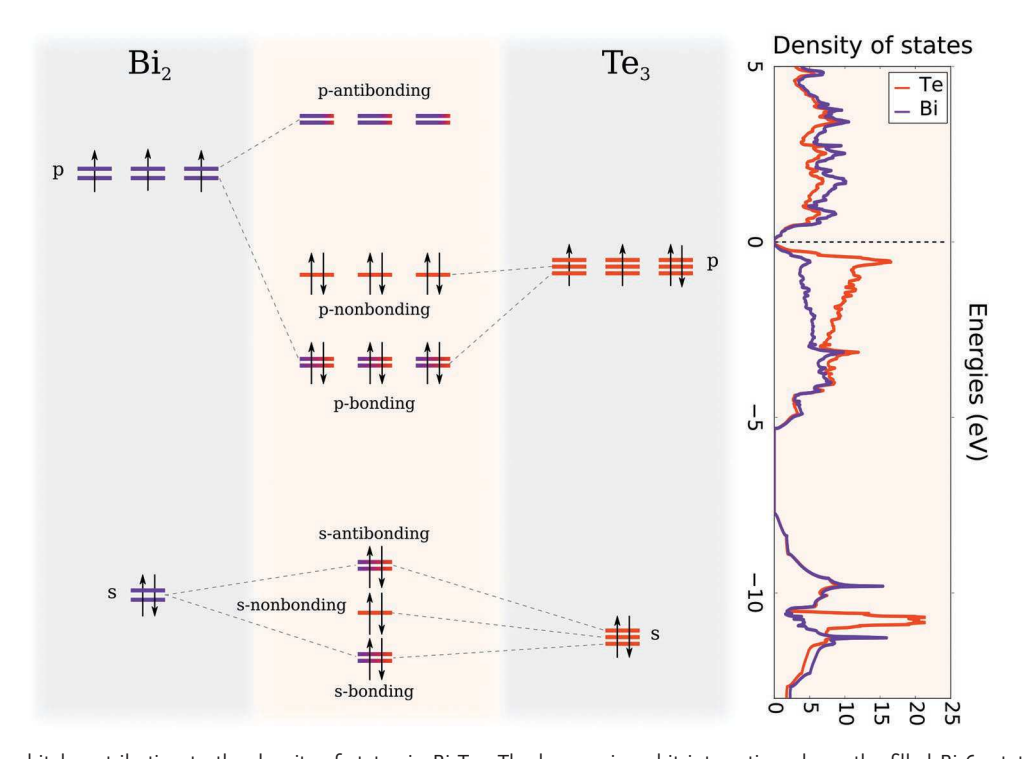


Figure 2. Atomic orbital contribution to the density of states in Bi₂Te₃. The large spin-orbit interaction places the filled Bi 6s-states far below the Te 5p-states. This makes the Bi octahedral coordination energetically favorable and leads to the formation of a lone pair on the Te⁽¹⁾ atoms. [180] The conduction band derives from the empty Bi—Te antibonding p-states with slightly stronger character from the more electropositive Bi states. The corresponding filled Bi—Te bonding p-states (with stronger Te character) make up part of the valence band. The valence band is also influenced by the less hybridized, nonbonding Te states from the van der Waals gap.

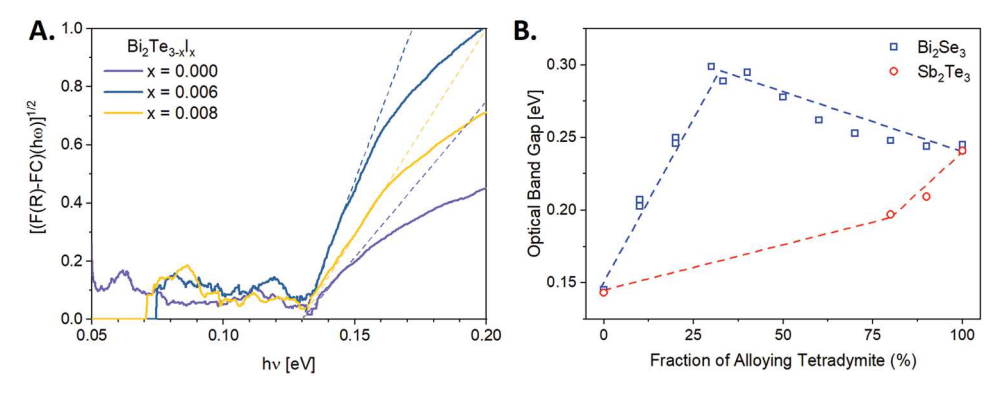


Figure 3. Optical bandgap for Bi_2Te_3 and its alloys with Bi_2Se_3 and Sb_2Te_3 . A) Measurement of the optical absorption coefficient and corresponding linear extrapolation for undoped and two I-doped Bi_2Te_3 samples finds a gap of 0.13 eV. B) Alloying with $Bi_2Se_3^{[63]}$ or $Sb_2Te_3^{[181]}$ increases the gap and can be beneficial for reducing the negative effects of thermally generated carriers.

Bismuth telluride has a narrow indirect gap of 0.14 eV as measured by room temperature optical absorption (**Figure 3**A) and transmittance. Unlike the more ionic lead chalcogenides, the bandgap of Bi_2Te_3 decreases with temperature like most covalent semiconductors at a rate of $0.95 \cdot 10^{-4} \, \text{eV} \, \text{K}^{-1}$.

Spin–orbit interaction (SOI) plays a critical role in making the band structure of Bi_2Te_3 complex by positioning the band extrema away from high symmetry points in the Brillouin zone. [4,5,50] Without SOI inclusion, calculations predict that Bi_2Te_3 should have a direct gap at the Γ -point with conduction and valence bands primarily comprised of Bi 6p and Te 5p states, respectively. [45,50,51] Instead, at the Γ -point the SOI reduces the energy of the Bi p-states more than those of Te so that the conduction band becomes lower in energy and crosses the valence band causing a band inversion (Figure 4). The strong interaction of these bands results in an avoided crossing that opens a new gap slightly displaced from Γ . This interaction naturally leads to small bandgaps, somewhat nonparabolic – almost linear bands that have small effective masses and high valley degeneracy as the direct bandgap has moved off the high symmetry Γ point.

This same SOI induced band inversion is also what makes Bi₂Te₃ and other tetradymites TI and is part of the reason why many TI materials are also TE materials. [4,50,52-56] The combination of inversion symmetry and SOI induced band inversion creates topologically protected surface states with time-reversal symmetry. [55] At the surface where inversion symmetry is broken, the surface band structure must have a connection between valence and conduction bands and forms a Dirac cone. [57] These surface states have their spin locked with their momentum which causes application of an electric field to produce a spin-polarized current. The magnitude and direction of the spin-polarization of the current can be tuned through controlling the Fermi level.^[58] Observation of the special behavior of topological surface states requires an insulating bulk. Bismuth telluride itself is a poor TI as native defects make reducing the bulk conductivity difficult. Furthermore, the surface state Dirac point lies below the bulk valence band maximum in energy making it impossible to separate TI behavior from the bulk conduction with a Fermi level near the Dirac point.^[4] The band structure and defect

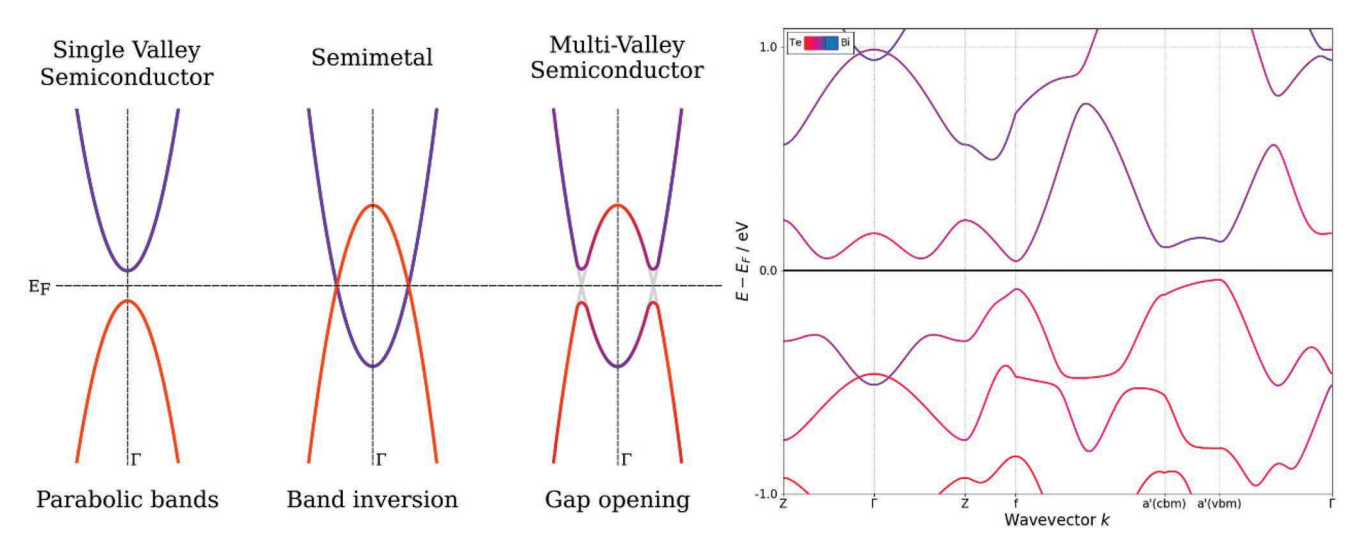


Figure 4. Origin of complex band structure in Bi_2Te_3 . Spin–orbit interaction closes the gap, causing the band inversion. As the states mix and an anticrossing occurs, a new gap opens, producing nonparabolic extrema away from Γ. This effect is integral to the band structure of Bi_2Te_3 and clearly visible at Γ when plotted along key directions showing band extrema.

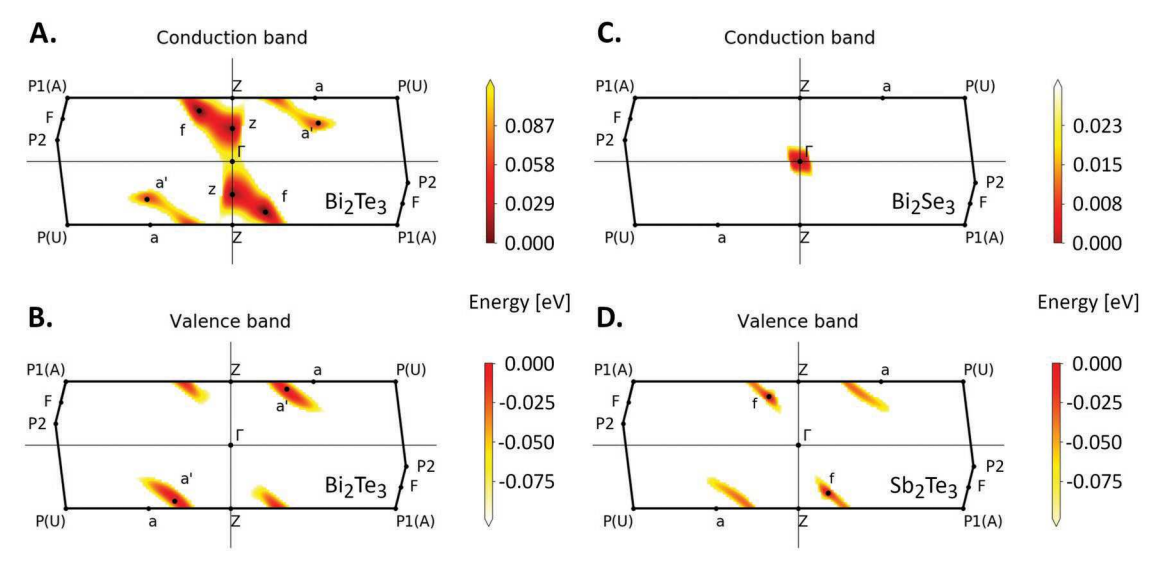


Figure 5. Bisectrix maps of Bi_2Te_3 conduction (A) and valence (B) band Fermi surfaces along with relevant surfaces from the typical alloying tetradymites: (C) Bi_2Se_3 and (D) Sb_2Te_3 . All transport relevant band edges are located within the bisectrix plane (highlighted in the BZ) Energies given are above or below the band extrema (CBM or VBM).

profile can be tuned for better TI behavior by alloying Bi_2Te_3 with Bi_2Se_3 or $Sb_2Te_3.^{[52,59-61]}$

The symmetry of the crystal structure requires the conduction band minimum (CBM) and valence band maximum (VBM) to lie on the bisectrix (mirror plane) of the Brillouin zone (Figure 5) which facilitates locating the band extrema when they are not along high symmetry directions shown in the band diagram^[62,63] (Figure 4). Band structure calculations for Bi₂Te₃ have yielded conflicting results about the exact position and therefore degeneracy of the band extrema largely because of the SOI induced sensitivity to the calculation details.[35,37,45] The complex interaction of this sensitivity with the specific combination of calculation method, exchange-correlation functional, and lattice parameters may explain the lack of consensus in the literature. As the bandgap is formed by the inversion and anticrossing at Γ , the position of band extrema depends on the details of both the CB and VB and their relative energy separation. Considering that the bands could move ≈0.1 eV with typical changes in temperature or doping for thermoelectric use, [49,64] the most relevant band structure may not be the most accurate at 0 K. The band diagram of Figure 4 and corresponding energy maps of Figure 5, which include SOI effects, were chosen primarily because they give results closest to experimental observations. While many studies have found that the lowest conduction band in Bi₂Te₃ is located at z along the Γ –Z line, a twofold degenerate point, [36,37,45,50] most recent studies^[5,35,36,46,62,65-67] have shown that the SOI shifts both the CBM and VBM to a general position within the bisectrix plane (CBM at f-point and VBM at a' point in Figure 5), which creates sixfold degenerate Fermi surface pockets. Band diagrams for Bi_2Te_3 are often plotted along the Γ -a line where a is a point between Z and P(U) despite the band maximum not being exactly at a. The Bi₂Te₃ CBM at f was first described on the path from Γ -F.^[62] Sb₂Te₃ has its VBM at f (Figure 5) in contrast to the VBM of Bi₂Te₃ at a'. Bi₂Se₃ has both its CBM (Figure 5) and VBM at Γ .[5,68]

In both n- and p-type Bi₂Te₃ and p-type Sb₂Te₃, the Fermi surfaces (Figure 6) at low doping are approximately ellipsoidal with sixfold degeneracy but rapidly become increasingly complex with higher Fermi energy, easily within reach by normal doping and operation temperatures of thermoelectric Bi₂Te₃ and Sb₂Te₃. The Bi₂Te₃ valence band Fermi surface starts with a sixfold degenerate pocket (Figure 6A) at the a' point (Figure 5). This pocket elongates (Figure 6B) toward f (Figure 5) upon doping. As the Fermi level is further increased, the pockets link together creating a ring structure around Z (Figure 6C). The Sb₂Te₃ valence band is reversed: emerging at the f point, then growing toward a' (Figure 5), however no ring formation at Zis observed and instead the pockets elongate and merge at Γ .^[5] We note that the details of the band structure calculation can cause the location of the VBM to be flipped from that presented here between a' and f for Bi₂Te₃ and Sb₂Te₃.^[5]

In the conduction band, as doping is increased, the sixfold (Figure 6D) pockets at the f point in the BZ (Figure 5) grow and a second twofold degenerate pocket appears at z. Upon further doping, the f pockets merge with the z pockets to form tripod structures (Figure 6E) which has been experimentally observed using ARPES.^[56] Similar structures are expected for the conduction band of $\mathrm{Sb_2Te_3}$.^[5] At even higher energies (Figure 6F) an additional sixfold degenerate pocket is found in the region near a' of the valence band.

Measurements of the band structure in Bi_2Te_3 , by galvano-magnetic, $^{[69-72]}$ de Haas-van Alphen, $^{[39,72,73]}$ and Shubnikov-de Haas (SdH) $^{[40,41]}$ effects have suggested that the both the CBM and VBM are sixfold degenerate and nonparabolic consistent with the description above for CBM at f and VBM at a'. $^{[35,36]}$ The degeneracies and Fermi surfaces of the CBM and VBM have also been confirmed more recently by angle-resolved photo-emission spectroscopy (ARPES). $^{[56,74,75]}$ The SdH measurements taken below 4 K also confirm the presence of a second conduction band (presumably at a' or z) offset 25 meV above the lowest conduction band, as well as a second valence

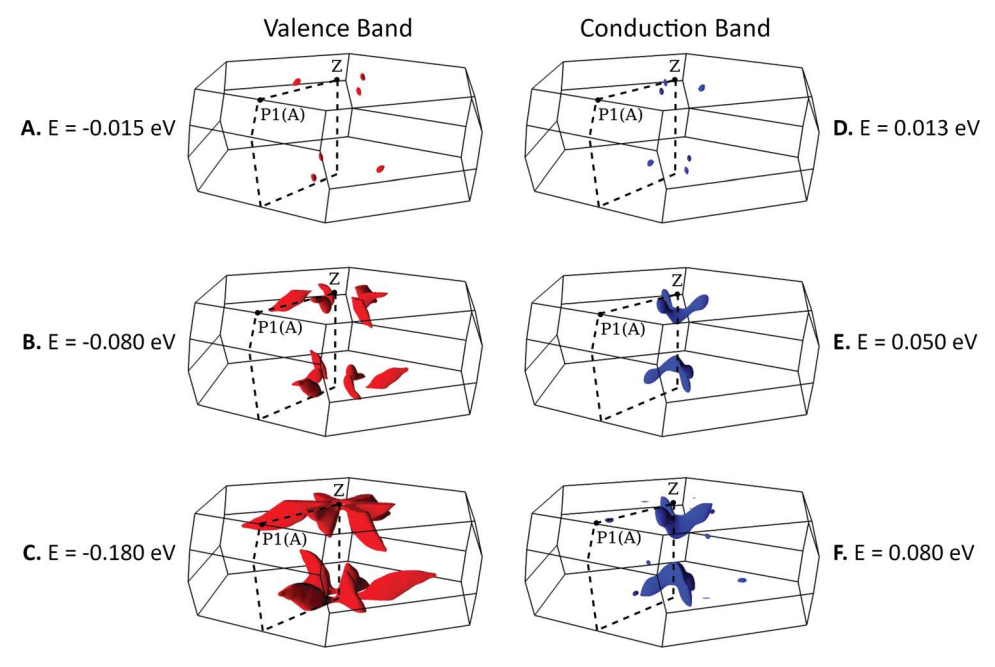


Figure 6. Valence and conduction band Fermi surfaces of Bi_2Te_3 . As Fermi level moves into the valence band, a sixfold ellipsoidal pocket A) grows across the BZ edge from a' to f B) and eventually merge forming a ring like structure around Z C). The conduction band also begins as a sixfold ellipsoidal surface D) until a twofold pocket emerges at z and combine to form a double tripod shape E). At still higher energies, an additional sixfold pocket emerges at a' F). These complex Fermi surfaces with high valley degeneracy contribute to the exceptional electrical thermoelectric performance of Bi_2Te_3 .

band (presumably at f) offset 20 meV below the highest valence band. Both additional bands are believed to have larger effective masses, but exact values have not been accurately determined. The heavier secondary bands are lying only a few $k_{\rm B}T$ apart from the primary ones at liquid helium temperatures but may shift at room temperature. $^{[40,41,43,76]}$ Optical measurements of the bandgap have shown an increase of $9.5 \cdot 10^{-5}$ eV K $^{-1[48]}$ when cooling down to \approx 120 K and the position and shape of band extrema may shift as well. $^{[48,63]}$ Similar changes in band energies with temperature are observed in the lead chalcogenides. $^{[49]}$

Alloying Bi₂Te₃ with Sb₂Te₃ has been suggested to shift the relative positions of highest energy valence bands,^[5,6] enabling band engineering to achieve band convergence similar to that used in the lead chalcogenides.^[7,77] Mixtures with Bi₂Se₃ and Sb₂Te₃ both increase the bandgap from that of pure Bi₂Te₃. The bandgap variation with composition abruptly changes slope at an intermediate point (Figure 3B) due to the relative movement of multiple band edges with changing composition. Further details of the effect of alloying will be discussed below in Section 3.

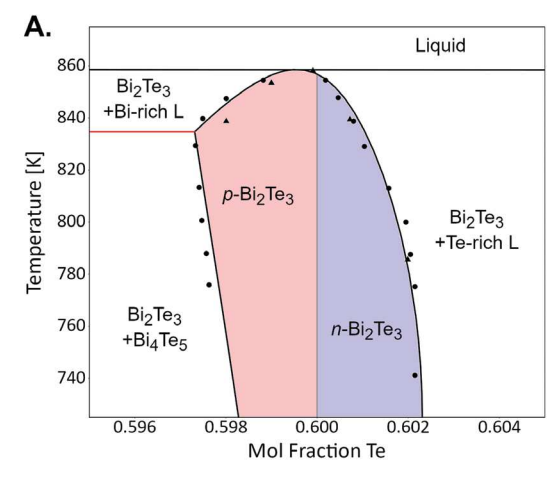
2.3. Defects and Doping

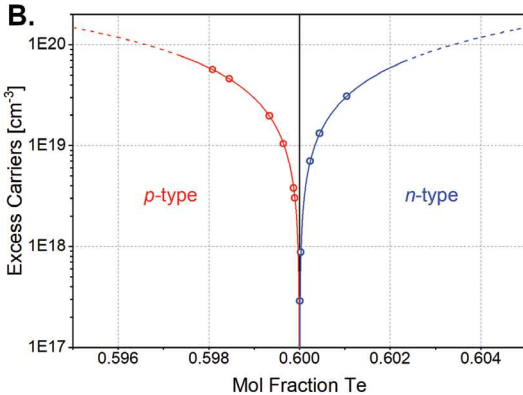
The carrier concentration in $\mathrm{Bi_2Te_3}$ and its alloys needs to be tuned to optimize zT for $\mathrm{cooling^{[78]}}$ or for power generation. Donor defects, such as I on at Te site, donate extra electrons or in the case of Se vacancy, accept fewer electrons into the valence band than without the defect. These simple defects can be understood by assigning a valence state based on the number of valence electrons and number of electrons

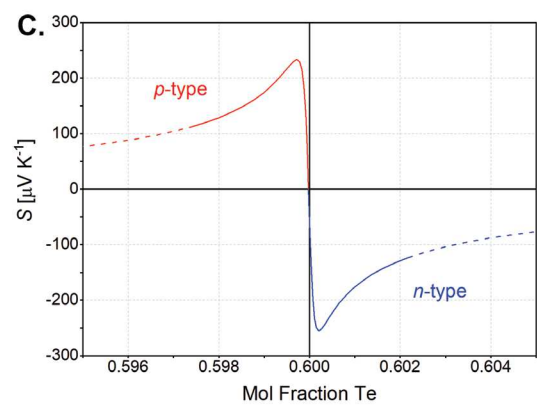
needed to fill valence states. For example, replacing Te^{-2} with I^{-1} produces one e^- ; an Sb on an anion site is Sb^{-3} which accepts one more electron than Te^{-2} and therefore produces a hole; whereas a Se^{-2} vacancy fails to accept two electrons and therefore is a two e^- donor.

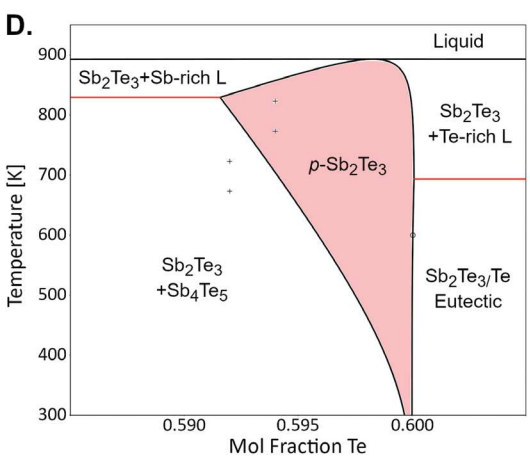
The conduction type and carrier concentration result from self-doping by antisite defects in nominally undoped binary Bi₂Te₃ and Sb₂Te₃, where electronegativity and atomic size differences are small, and anion vacancies in the case of Bi₂Se₃ where these differences are larger. [82] The concentrations of these native defects can be on the order of 10¹⁸–10¹⁹ cm⁻³ depending upon the composition and temperature at which the material was made or processed. [83,84] Since the nominal compound Bi₂Te₃ has a finite phase width, the defect concentrations will depend on the exact atomic chemical potentials of Bi and Te and defects for the two extreme cases, Bi-rich or Te-rich, are often reported in theoretical studies.[85] Whereas vacancies are the dominant intrinsic defects in PbTe, precise density measurements[86] as well as theoretical calculations^[59,60] have shown that antisite defects control the intrinsic charge carrier concentration in Bi₂Te₃. Thus, while Pb-rich PbTe is n-type, Bi-rich Bi₂Te₃ is p-type due to Bi_{Te} antisite acceptor defects. Bi replaces Te with a similar electronic structure but one less electron producing a hole in the valence band. Similarly, a Te on Bi site has the same electronic structure but one more electron making TeBi an electron donor and is the dominant defect under Te-rich conditions.[82]

As shown in **Figure 7**A, the congruently melting point of bismuth telluride is shifted slightly toward the Bi side of the Bi₂Te₃ composition. Thus a solid grown from an exactly stoichiometric melt will actually be Bi-rich and p-type.^[83,87] Depending on the growth and processing conditions (e.g., liquidus composition









during growth or annealing in controlled Bi-rich or Te-rich conditions), $^{[28,84,88]}$ a range of stoichiometry between 59.8 and 60.2 at% Te can be prepared. $^{[87]}$

The comparatively low formation energy of Sb_{Te} antisite defects causes Sb_2Te_3 to always be p-type. This occurs even in Te-rich Sb_2Te_3 which although containing fewer Sb_{Te} defects than Te-rich Sb_2Te_3 remains strongly p-type (Figure 7D). Bi_2Se_3 in contrast has sufficiently low formation energy for selenium vacancies to make the material always n-type. [59,60,82]

In the case of binary Bi₂Te₃ the antisite defect concentrations can be adjusted with processing conditions (Bi- or Te-rich and temperature) only up $\approx 5 \times 10^{19}$ cm⁻³ (Figure 7B, either n-type or p-type), but by isoelectronic alloying (with Sb₂Te₃ or Bi₂Se₃) a greater range of carrier concentrations is achievable by manipulating the defect chemistry. For example, the replacement of some Bi with Sb leads to the strong favoring of Sb_{Te} acceptor defects such that the hole concentration of p-type (Bi,Sb)2Te3 alloys can be adjusted via the Bi/Sb ratio. [82] In principle the hole concentration should vary depending on whether the preparation is metal-rich or Te-rich by an amount similar to that observed in binary Bi₂Te₃ or Sb₂Te₃. In practice, this effect has not yet been documented with a complete phase boundary mapping study. [85] Similarly, the electron concentration of n-type Bi₂(Te,Se)₃ alloys can be controlled for Bi₂Se₃ amounts higher than 33%.[89,90] In this case the Bi-rich conditions which will increase the donor Se vacancy defects will also promote the Bi_{Te} acceptor defects. Such counteracting effects between different point defects can lead to profoundly different properties for the different thermodynamic states (e.g., cation-rich or chalcogen-rich) and therefore inhomogeneous material when the processing does not clearly define the thermodynamic state.

Like conventional semiconductors, the charge carrier density in Bi₂Te₃ can also be adjusted by extrinsic doping. Tuning of the carrier concentration is straightforward by aliovalent substitutions (substitution by atoms with one more electron (donors) or one fewer electrons (acceptors)). Halogens are ideal donors when substituting for tellurium as they contribute one extra electron and should less disrupt the conduction band compared to cation-site dopants as found in the lead chalcogenides.^[91] Similarly, lead is an ideal acceptor as it replaces bismuth with one less valence electron while still possessing a filled s-state. [92] Group II elements such as calcium, without the filled s-state, also substitute on the cation site forming one electron acceptor defects.^[93] The carrier concentration is determined by the net effect of the different sources of doping owing to the interaction of the extrinsic impurities with the intrinsic point defects enabling ternary, quaternary and more complex compositions to be tuned from intrinsic to highly extrinsic carrier concentrations.^[31,94–98]

Figure 7. Thermodynamic and thermoelectric phase diagrams of Bi_2Te_3 . A subsection of the Bi—Te binary phase diagram A) illustrates the range of solubility for Bi_2Te_3 that results from low antisite defect formation energies for each element. $^{[182]}$ The concentration of antisite defects and thus solid composition can be inferred from Hall measurements $^{[83]}$ to estimate carrier concentration as a function of composition B). Using appropriate models (Figures 9 and 10), this can be extended to predictions of the Seebeck coefficient with composition C) and extreme sensitivity to stoichiometry near 60 at% Te is observed. A similar phase diagram for Sb2Te3 D) reveals a strong tendency for SbTe antisite formation and results in Sb2Te3 always being p-type. $^{[182]}$



In ${\rm Bi_2Te_3}$ at typical operating temperatures and carrier concentrations for thermoelectric purposes, the choice of aliovalent dopant does not appear to have a significant impact on transport because deformation potential scattering dominates (see Section 3.2). Such differences are usually only observed in other semiconductors at very high carrier concentrations, e.g., $\approx 10^{19} {\rm \, cm^{-3}}$ at 300 K in n-type Si doped with P, As, or Sb.^[99]

If the dopant, however, modifies the electronic structure, then it can also be a mechanism for engineering the electronic properties. Figure 10 illustrates how for most dopants, the Seebeck and Hall mobility follow expected trends with Hall carrier concentration with tin being the notable exception. While in the same group as lead, tin is a so called "resonant dopant" and produces a noticeably larger Seebeck coefficient for a given carrier concentration within a specific range of doping.[9,100-102] This is because the tin 5s orbital states introduce a small peak in the density-of-states near the top of the valence band. [8,103] While the increase in Seebeck coefficient may appear advantageous, it is accompanied by a decrease in carrier mobility which negates potential gains in power factor (Figure 10B). Tin is an important dopant in tetradymite topological insulators where it can aid in more predictable carrier concentration tuning to reduce bulk conductivity.[103,104]

Various processing methods have also been observed to create electrically active defects in polycrystalline Bi₂Te₃ that could be due to charged defects at nonequilibrium grain boundary or extended defects, or unknown impurities.^[105] For example, deformation such as grinding,[106] high energy ball milling,[107,108] or electrochemical deposition[109] can produce a donor-like effect. Annealing or other high temperature processing (e.g., high temperature hot deformation^[105] or spark plasma sintering^[107,110]) can reduce but may not eliminate the doping effect. In such processed materials, the carrier concentration can be altered significantly enough to even cause the dominant charge carrier type to invert relative to the as grown compositions.[82,111] Second phase particles can also impact the carrier concentration. Nominally inert impurities, such as SiC particles used to control grain microstructure can also have an effect on charged defects.[112] The competition and interaction of these intrinsic and extrinsic dopants makes tuning the Fermi level a complex procedure. [82]

3. Thermoelectric Transport of Bi₂Te₃ and Related Compounds

3.1. Quality Factor and zT

The exceptional thermoelectric performance of Bi_2Te_3 near room temperature is due to its complex electronic structure and relatively low thermal conductivity which gives it a high thermoelectric quality factor, B. While the maximum thermoelectric efficiency of a given sample is determined by the figure of merit $zT = S^2\sigma T/\kappa$ (where S is the Seebeck coefficient, σ is the electrical conductivity, κ is the thermal conductivity and T is the temperature) the maximum zT of a dopable semiconductor is determined by the thermoelectric quality factor, B, defined in Equation (1).[113,114]

$$B = \left(\frac{k_{\rm B}}{\rm e}\right)^2 \frac{8\pi \rm e \left(2m_e k_{\rm B}\right)^{3/2}}{h^3} \frac{\mu_{\rm w} T^{5/2}}{\kappa_{\rm L}} = 4.33 \cdot 10^{-10} \frac{\mu_{\rm w} T^{5/2}}{\kappa_{\rm L}} \tag{1}$$

$$B = \frac{2k_{\rm B}^2\hbar}{3\pi} \frac{C_1 N_{\rm v} T}{m_{\rm t}^* \Xi^2 \kappa_1} \tag{2}$$

Here $\mu_{\rm w}$ is the weighted mobility with units of m² V⁻¹ s⁻¹, which characterizes the relationship between the Seebeck coefficient and electrical conductivity and can be used to estimate the variation of power factor with doping. The lattice thermal conductivity, κ_1 , with units of W m⁻¹ K⁻¹ quantifies the heat transport by phonons. [115-117] The B of a material type such as Bi₂Te₃ depends on the electronic and atomic structure and electron and phonon scattering of the material. This is more clearly seen in the form of B where $\mu_{\rm w}$ has been expanded to its constituent parameters using Equation (S19) in the Supporting Information: valley degeneracy N_v , inertial effective mass m_1^* , deformation potential Ξ , and average longitudinal elastic modulus C_1 . The combination of these parameters determines the highest achievable figure of merit zT for the case where the material is optimally doped and the bandgap is sufficiently large enough that bipolar effects are not present (Figure 8). As a useful point of reference, to attain a zT of 1 a B > 0.4 is required.

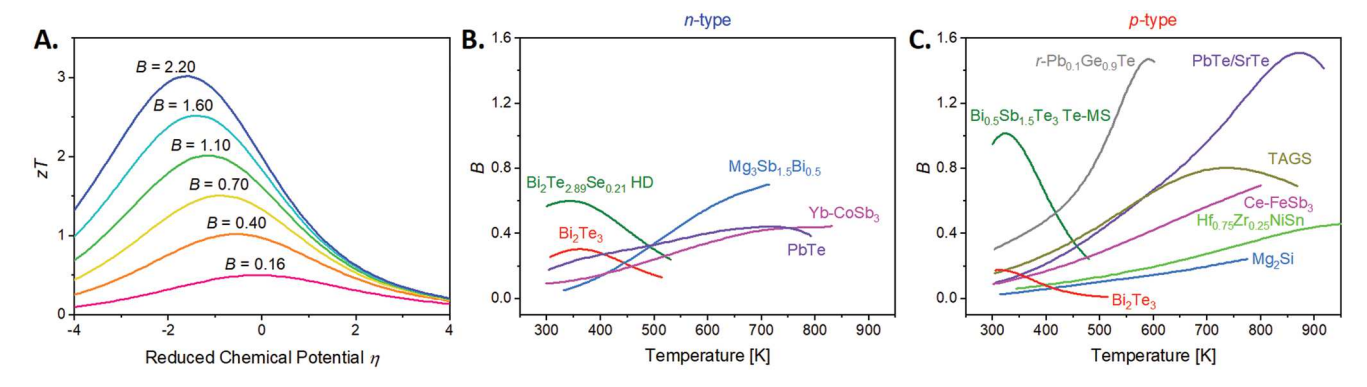


Figure 8. The material quality factor B allows for comparison of potential zT between samples and different materials without doping dependence A). Comparison with other notable thermoelectric materials demonstrates how exceptional both B) n- and C) p-type Bi_2Te_3 and its alloys are near room temperature. [11,122,123,183–191]



www.advancedsciencenews.com



The crystalline anisotropy of $\mathrm{Bi_2Te_3}$ and its alloys complicates the transport property measurements and adds uncertainty to the values reported. Because the conductivity anisotropy ratio (higher within the basal ab planes) exceeds that of the lattice thermal conductivity, the thermoelectric transport parallel to the basal planes leads to higher zT. The Seebeck coefficient, depending more on scalar quantities such as E_F and density of states mass, is more isotropic. For this reason, the thermoelectric properties of $\mathrm{Bi_2Te_3}$ discussed below and quality factors tabulated in Table 1 for comparison with other materials are only given for measurements along ab directions of large oriented grains (e.g., by zone melting).

3.2. Thermoelectric Transport Properties of Bi₂Te₃

The electronic transport of Bi₂Te₃ can be generally described as that of a small bandgap semiconductor where the conduction band has somewhat higher mobility than the valence band but the Seebeck effective masses are nearly the same. Despite the complexity of its electronic structure, valuable insight can be obtained from a quantitative analysis of the thermoelectric transport in Bi₂Te₃ in terms of the material parameters that make up *B*: Seebeck effective mass m_5 *, weighted mobility $\mu_{\rm w}$ and lattice thermal conductivity $\kappa_{\rm l}$. These parameters are common topics for experimental and theoretical study in themselves and thus naturally lead to strategies for their manipulation toward improving material properties.

When the electrical conductivity is low, σ below ≈ 500 S cm⁻¹, there is a sharp reduction of thermopower |S| and change in sign which corresponds to the intrinsic regime where carriers in both conduction and valence bands contribute significantly to transport. The opposing Seebeck effect from each carrier type results in the dramatic reduction of overall thermopower at low, σ . The effects of mixed conduction are significant even at room temperature as seen by the difference between the single band (dashed lines) and conduction + valence band models (solid lines) of **Figure 9**. The two-band model (see the Supporting Information) requires an energy gap of 0.14 eV, which is in good agreement with the optically measured bandgap (Figure 3A).

3.2.1. Effective Mass Modeling of Room Temperature Thermoelectric Properties

The parameters required to model the conduction and valence bands are derived from the data in the extrinsic regime (σ greater than $\approx 1000~\rm S~cm^{-1}$). The variability in samples and/or measurements from the many different studies compiled in Figure 9 make it is difficult to identify consequences of the complex Fermi surface, multiple nonparabolic bands^[40,41] and various scattering mechanisms^[31] in the charge carrier transport generally observed in Bi₂Te₃. The general trends observed in Figure 9 can be characterized by a simple, single weighted mobility for each carrier type (dashed lines). The somewhat higher weighted mobility for electrons ($\mu_w = 525~\rm cm^2~V^{-1}~s^{-1}$, Table 1) compared to holes (400 cm² V⁻¹ s⁻¹) gives larger power

factor ($S^2\sigma$ Figure 9B) for n-type materials (\approx 45 μ W cm⁻¹ K⁻²) while p-type samples reach only \approx 35 μ W cm⁻¹ K⁻². This may be contrary to expectation as p-type Bi₂Te₃ alloys are known to exceed their n-type counterparts in zT. As discussed in Section 2.1, the discrepancy arises due to the greater anisotropy in mobility of n-type materials which negates much of the benefit of microstructure engineering to reduce thermal conductivity.^[1]

For samples with carefully characterized Hall coefficient a separate Hall mobility $\mu_{\rm H}$ and Seebeck effective mass $m_{\rm S}^*$ (akin to density-of-states mass) can be extracted from the variation of Seebeck coefficient with the Hall carrier concentration (**Figure 10**A). [114] At 300 K a similar value for the Seebeck effective mass of 1.06 $m_{\rm e}$ is found for both n-type and p-type charge carriers and agrees well with similar analyses in other studies. [120,121] These effective $m_{\rm S}^*$ values, derived from experimental Seebeck and Hall measurements are an ideal way to characterize changes to the band structure or compare to other materials. [6,122,123] However, these experimental values are not expected to match other definitions of m^* as the Seebeck and Hall effects will be affected by the complex band structure and scattering, [33,116,124–126] as well as Hall effect depending on crystal and magnetic field orientation. [31,32,70,116,127]

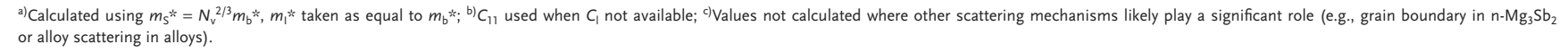
The effective deformation potential Ξ (Table 1) of 22 eV for electrons and 25 eV for holes for phonon scattering may also be a useful parameter for comparison. Here we assume deformation potential phonon scattering dominates and use $C_1 = 68 \text{ GPa}^{[128]}$ and $N_v = 6$ although the number of valleys and extent of intervalley scattering is actually unknown. The slightly larger value for holes accounts for the lower weighted mobility and the subsequently the lower thermoelectric quality factor.

An average lattice thermal conductivity κ_L of 1.37 W m⁻¹ K⁻¹ (300 K) for single crystal Bi₂Te₃ is found by extracting the electronic contribution to κ . The total thermal conductivity, κ , (Figure 9C) varies with electrical conductivity approximately linearly in the extrinsic regime with a sharp increase in the intrinsic region attributed to the bipolar thermal conductivity. Comparison of the two-band model (solid lines) and single band extrapolation (dashed lines) shows that bipolar thermal conductivity contributes even above $\sigma \approx 1000 \text{ S cm}^{-1}$. Without consideration of the mixed conduction effects, higher estimates of the lattice thermal conductivity are expected - reported values for $\kappa_{\rm L}$ are between 1.4 and 1.7 W m⁻¹ K⁻¹ for Bi₂Te₃. [83,84,92,116] The minimum thermal conductivity is even lower 0.2–0.3 W m⁻¹ K⁻¹ predicted by diffusion^[129] and Cahill's model^[130] demonstrating the potential for improvement in zT through microstructure engineering.

The reported room temperature zT values of n- and p-type Bi₂Te₃ (Figure 9D) are quite scattered, requiring the transport models to provide clarity. Given the trends in thermal and electrical properties, the zT of p-type Bi₂Te₃ is expected to peak at 0.5–0.6 for an electrical conductivity between 900 and 1100 S cm⁻¹. The maximum zT for n-type Bi₂Te₃ is expected around 0.7, where slightly higher values are reported. For both conduction types, the zT from the two-band model is lower in magnitude and shifted toward higher conductivity than what is predicted from a single band model because of the high bipolar thermal conductivity below ≈ 1500 S cm⁻¹ which is a consequence of the small bandgap in Bi₂Te₃.

Table 1. Comparison of key transport parameters for notable thermoelectric materials at 300 K. Key: weighted mobility μ_{w_0} lattice thermal conductivity κ_L , thermoelectric quality factor B, bandgap E_g , mobility parameter μ_0 , Seebeck (DOS) effective mass m_S *, single valley band mass m_b *, average longitudinal elastic modulus C_0 , acoustic phonon deformation potential Ξ , static dielectric constant ε .

Material	$\mu_{\rm w} [{\rm cm^2 V^{-1} s^{-1}}]$	$\kappa_{\rm L}$ [Wm $^{-1}$ K $^{-1}$]	В	E _g [eV]	Goldsmid-Sharp $E_{\rm g}$ [eV]	$\mu_0 [{\rm cm^2 V^{-1} s^{-1}}]$	m _S * [m _e]	$N_{\rm v}$	$m_{\rm b}^{\star~a)}$ [$m_{\rm e}$]	C _I ^{b)} [GPa]	Ξ ^{c)} [eV]	$\varepsilon\left[arepsilon_{0} ight]$	Ref.
Bi ₂ Te ₃ (n)	525	1.37	0.26	0.14	0.14	481	1.06	6	0.32	68	22	290 ⊥, 75	[63,145,194]
Bi ₂ Te ₃ (p)	400	1.37	0.20	0.14	0.14	367	1.06	6	0.32	68	25	290 ⊥, 75	[63,132,145,194]
Bi ₂ Se ₃ (n)	165	1.70	0.07	0.30		1403	0.24	1	0.24	74	11	113 ⊥	[54,139,194]
Sb ₂ Te ₃ (p)	465	2.20	0.14	0.24		675	0.78	6	0.24	55	25	168 ⊥, 37	[6,28,144,181,195]
$Bi_2Te_{2.79}Se_{0.21} HD$ ZM (n)	463	0.56	0.56	0.19	0.17	252	1.50	6	0.45	68			[63,145,185]
$Bi_{0.5}Sb_{1.5}Te_3$ Te-MS (p)	490	0.35	0.94	0.20	0.18	425	1.10	6	0.33	57			[6,11,181]
PbS (n)	160	2.50	0.04	0.37		609	0.41	4	0.16	111	27	169	[113,144,196]
PbSe (n)	160	1.70	0.06	0.26	0.38	1140	0.27	4	0.11	91	25	210	[113,144,196–198]
PbSe (p)	110	1.70	0.04	0.26	0.33	784	0.27	4	0.11	91	35	210	[113,144,196,197,199]
PbTe (n)	200	1.50	0.09	0.30	0.36	1509	0.26	4	0.10	71	22	414	[64,113,144,187]
PbTe (p)	100	1.50	0.04	0.30	0.43	754	0.26	4	0.10	71	25	414	[64,113,144,187,200]
Pb _{0.95} Sb _{0.05} Se (n)	40	0.70	0.04	0.26	0.35	285	0.27	4	0.11	91			[113,196,201]
PbTe+8% SrTe	237	1.71	0.09	0.34	0.48	136	1.45	4	0.58	71			[113,189]
TAGS-85 (p)	141	0.63	0.15		0.30								[190]
Pb _{0.1} Ge _{0.9} Te (p)	241	0.54	0.30			69	2.30	12	0.44	30			[122,202]
Mg ₂ Si (n)	147	4.56	0.02	0.71	0.62	99	1.30	3	0.62	121	22	19	[144,188,203–206]
Mg_3Sb_2 (n)	11	1.50	0.00			6	1.50	6	0.45	40			[85,186,207,208]
Mg_3Sb_2 (p)	8	1.50	0.00		0.47	12	0.80	1	0.80	40	19		[186,207–209]
$Mg_{3.2}Sb_{1.5}Bi_{0.5}$ (n)	47	0.88	0.04			32	1.28	6	0.39	40			[186,207,208]
CoSb ₃ (n)	83	8.65	0.01	0.22		142	0.70	3	0.34	95	36		[123,210]
CoSb ₃ (p)	235	8.65	0.02	0.22	0.20	3077	0.18	1	0.18	95	12		[123,210,211]
$Yb_{0.3}Co_4Sb_{12}$ (n)	362	1.88	0.13	0.22		64	3.17	15	0.52	95	53		[123,210]
CeFe ₄ Sb ₁₂ (p)	213	1.60	0.09										[183]
ZrNiSn (n)	121	4.75	0.02	0.13	0.2	18	3.57	3	1.72	119	15		[212–215]
ZrNiSn (p)	28	4.75	0.00	0.13	0.05	2	5.26	3	2.53	119	25		[212–215]
$Hf_{0.75}Zr_{0.25}NiSn$ (n)	329	4.84	0.05		0.31			3		110			[191,214,215]
Si (n)							1.18	6	0.36	167	6.5	11.9	[141,165,216]
Si (p)							0.81	3	0.39	167	11.3	11.9	[141,165,216]
InSb (n)									0.0016	79	30	17.6	[146,147]
InSb (p)									0.4	79	7	17.6	[146,196,216]







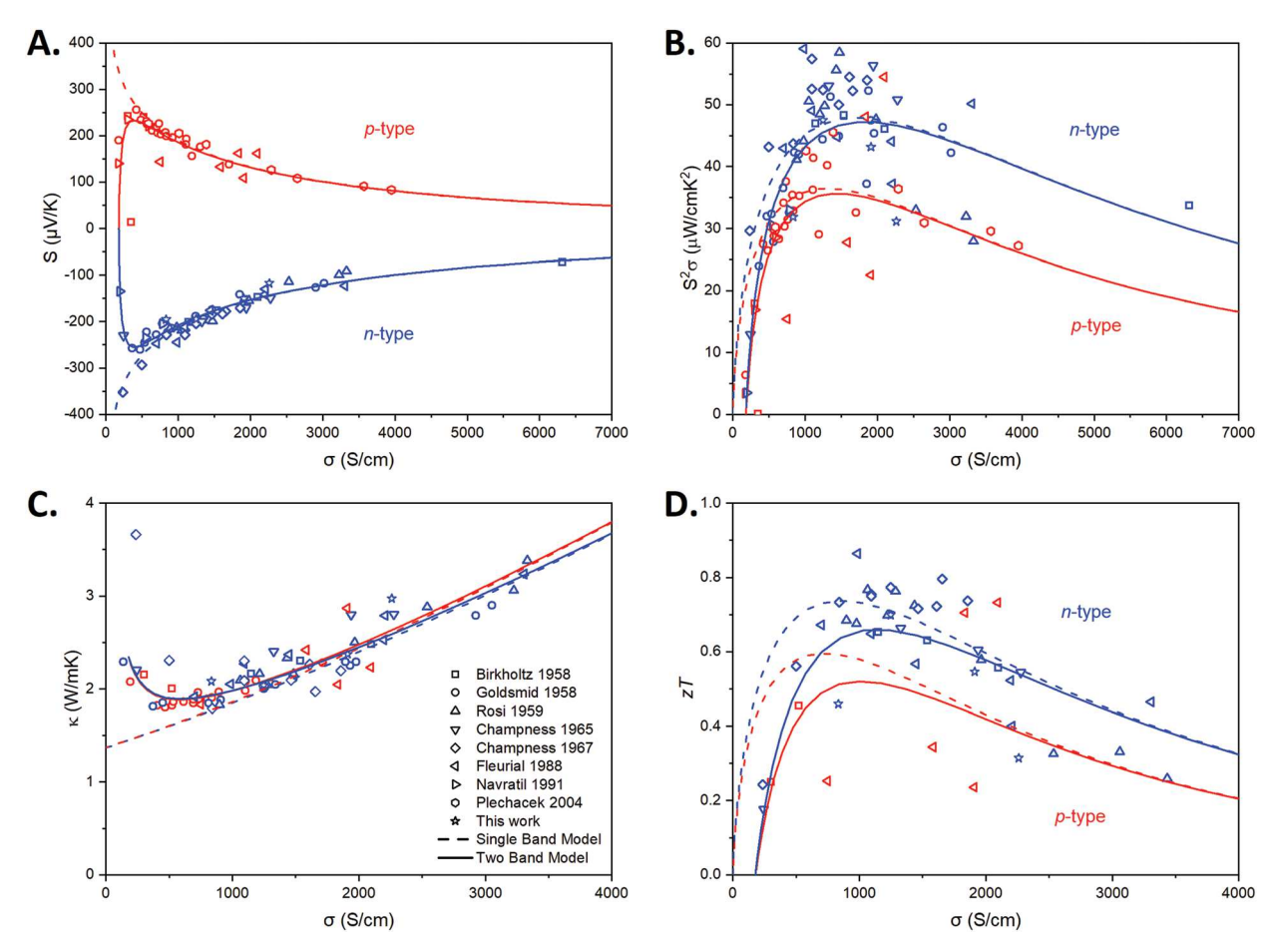


Figure 9. A survey of room temperature thermoelectric transport measurements of n- and p-type Bi_2Te_3 (along the *ab* direction) as a function of electrical conductivity. [21,79,117,125,127,133,165,166] Single (dashed) and two-band (solid) effective mass models describe the data well and illustrate the limiting effect of minority carriers at low conductivity values. At room temperature, the effect is small for the Seebeck coefficient A) and power factor B), but it is substantial for the thermal conductivity C). The bipolar effect can be comparable to a lattice thermal conductivity of 1.37 W m⁻¹ K⁻¹ and this limits the maximum achievable zT D). n-type Bi_2Te_3 has higher performance due to its μ_w of 525 cm² V⁻¹ s⁻¹ for electrons compared to 400 for holes.

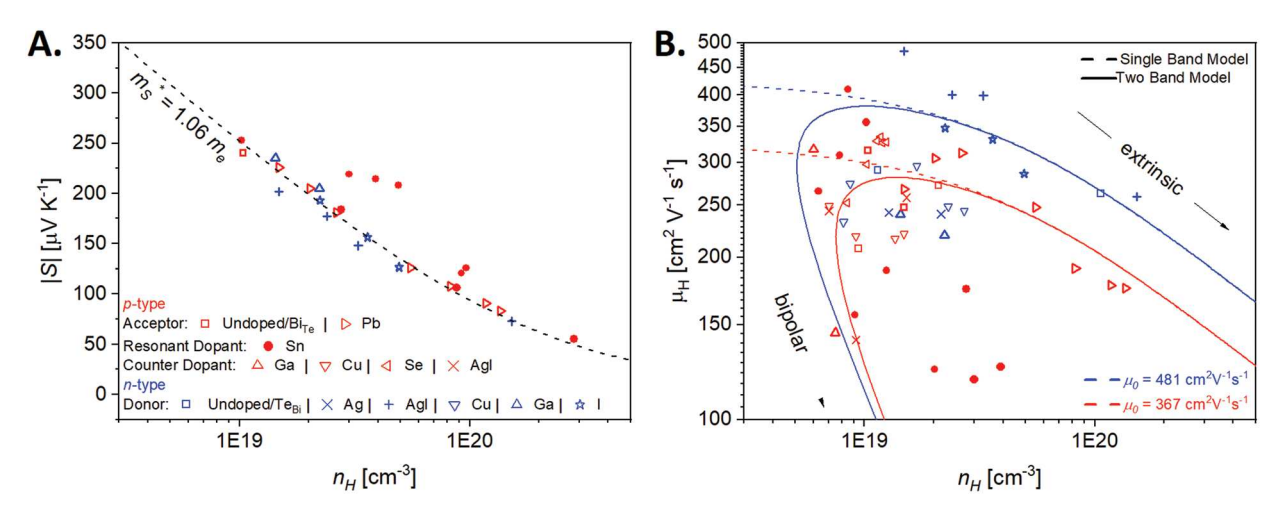


Figure 10. The room temperature Pisarenko plot of Seebeck versus Hall carrier concentration A) is well fit using a Seebeck effective mass of 1.06 m_e for n- and p-type Bi₂Te₃ (along the *ab* direction). [9,100,132,192] This mass along with the weighted mobilities used in Figure 9 and the 0.14 eV bandgap can be used to predict the Hall mobility versus Hall carrier concentration B). [94,98,100,101,132,137,192,193] The difference between the single-band (dashed line) and two-band models (solid line) illustrates the strong bipolar effects on the Hall data, and the apparent Hall mobility (not actual charge carrier mobility) at low dopant concentrations.

www.advancedsciencenews.com



3.2.2. Comparison to Other Thermoelectric Materials

Bi₂Te₂ and its alloys with Sb and Se have the highest known quality factor and weighted mobility near room temperature which is why this class of materials makes the best thermoelectrics. Bi₂Te₃ and Sb₂Te₃ show higher DOS (Seebeck) effective masses (m_S *) near 1 m_e (Table 1), while for the Bi₂Se₃ and the n-type Pb-chalcogenides $m_S^* \approx 0.2-0.3 m_e$. The higher effective mass is related to the larger band degeneracy (N_v) like that found in p-type Pb-chalcogenides. The higher valley degeneracy at room temperature helps make Bi and Sb-tellurides have higher $\mu_{\rm w}$ which leads to large power factors (Figure 12B). This, combined with the relatively low $\kappa_{\rm I}$ ultimately leads to higher thermoelectric quality factors and for Bi₂Te₃ and Sb₂Te₃ making them superior for room temperature applications. The small bandgap of Bi₂Te₃ prevents it from being useful at higher temperatures enabling other materials such as PbTe, B = 0.39 (at 650 K), and SiGe, B = 0.38 (at 1100 K). [131]

Bismuth telluride has a high weighted mobility partly due to its complex Fermi surface (due to spin-orbit interaction described above) that gives it two nearly degenerate sets of six-valley conducting bands which have a low inertial mass. [69,127] The small electronegativity difference between the elements and strong interaction between conduction and valence bands results in the low inertial mass and also a narrow bandgap. [25] In contrast conventional semiconductors with light elements generally have simpler conduction and valence bands at high symmetry points, while the tetradymites are more complex.

3.2.3. Temperature Dependent Transport Properties of Bi₂Te₃

Temperature dependent thermoelectric transport data is typically reported and analyzed to calculate zT and characterize scattering. Because of the variation in results from different studies, trends are best discussed about a series of samples prepared and measured the same way. Here, we limit our discussion to the I-doped n-type material produced for this work and the Pb-doped p-type $\rm Bi_2Te_3$ electrical transport results of Plecháček et al.[132]

The limiting effect of the small bandgap is observed in all electrical and thermal measurements (Figure 11). The magnitude of the Seebeck coefficient rises with temperature as the Fermi level moves toward the minority carrier band. Eventually the Seebeck peaks and drops as minority carriers are generated. The location and value of the Seebeck peak can be used to measure the bandgap^[133,134] and is found to be 0.14 eV. The Seebeck peak is shifted to higher temperatures (but at a lower value) with increased doping as it places the Fermi level further toward (or inside) the majority charge carrier band. This manifests in a reduction of the maximum achievable power factor with optimized doping with increasing temperature (Figure 12B). The figure of merit zT (Figure 11F) also peaks because of the peak in Seebeck and the rise in thermal conductivity. The highest observed zT = 0.7 in the I-doped samples of this work occurs near 325 K for the x = 0.006 sample.

The Hall coefficient (Figure 11C) is observed to decrease in magnitude in all samples with increasing temperature due to

canceling effect of the opposite signs of $R_{\rm H}$ for the holes in the VB and electrons in the CB. Thus, interpretation of the carrier concentration by $n_{\rm H}=1/eR_{\rm H}$ can potentially lead to erroneous overestimation of the true carrier density and underestimation of the true carrier mobility. Similarly, the temperature dependence of mobility (Figure 11D) is complex in both n- and p-type materials and care should be taken in when assessing the dominant carrier scattering mechanism. Multiple studies have found that above room temperature the primary mechanism is deformation potential scattering from acoustic or nonpolar optical phonons. [38,88,135-137] Deformation potential scattering predicts an exponent λ in $\mu_{\rm H} \approx T^{-\lambda}$ between 1.5 (nondegenerate) and $\lambda = 1$ (degenerate). The observed λ falls within a range of 1.1 and 2.8 and increases with temperature for all samples. As the Hall mobility is calculated by $\mu_{\rm H} = |R_{\rm H}|\sigma$, the reduction in $|R_H|$ due to thermal excitation of minority carriers will cause the Hall mobility to decrease faster with temperature than the true mobility of carriers. This effect can be significant even at room temperature in samples having lower carrier concentrations, as shown in Figure 10B. For example, Hall measurements at 300 K on p-type samples of equal crystalline quality with $n_{\rm H} = 10^{19} \, {\rm cm}^{-3}$ carriers could find Hall mobilities of ≈ 125 or ≈ 275 cm² V⁻¹ s⁻¹. This disparity in Hall mobility is not an indication of the degree of charge carrier scattering but instead of the position of the Fermi level and the indeterminate nature of the Hall coefficient when minority carriers play a significant role. This effect is likely contributing to the steep T-2.8 dependence observed in the more lightly doped Bi₂Te_{2 996}I_{0 004} sample near room temperature in Figure 11. To properly evaluate λ , the slope should be determined when the material is certain to be extrinsic. While low temperature data is unavailable for our I-doped samples, similar $T^{-2.8}$ dependence of Hall mobility has been reported at low temperatures for samples doped near 10¹⁷ cm⁻³ carriers with numerous other studies reporting λ values greater than the expected 1.5. [69,70,83,121,138] This suggests that minority carrier effects alone cannot explain the observed λ values.

The complexity of the band structure in Bi₂Te₃ can also play a role in the observed value of λ . If multiple band edges are involved in conduction, as is the case in both n- and p-type Bi₂Te₃,^[40,41] the measured mobility will depend on the relative contributions of each. This will depend on the energetic separation, the density-of-states and mobility of each band, and the position of the Fermi level determined by the doping and temperature. At a given temperature, the Hall mobility can therefore have a carrier concentration dependence that deviates from that expected by the degree of degeneracy. As the Fermi level shifts with temperature along with the width of the Fermi-Dirac distribution, the number of carriers in each band can vary even if the total carriers remain unchanged. Carriers moving from a high mobility band to a lower mobility band as a function of temperature will appear as a faster decrease in measured mobility and therefore higher λ than expected for a scattering mechanism. Thus, the observed λ could potentially differ from expectation for a scattering mechanism even if that mechanism dominates. Examination of Figure 11D suggests that in both conduction types, this multiple band effect increasing λ is occurring for samples with low doping and that at high doping both bands



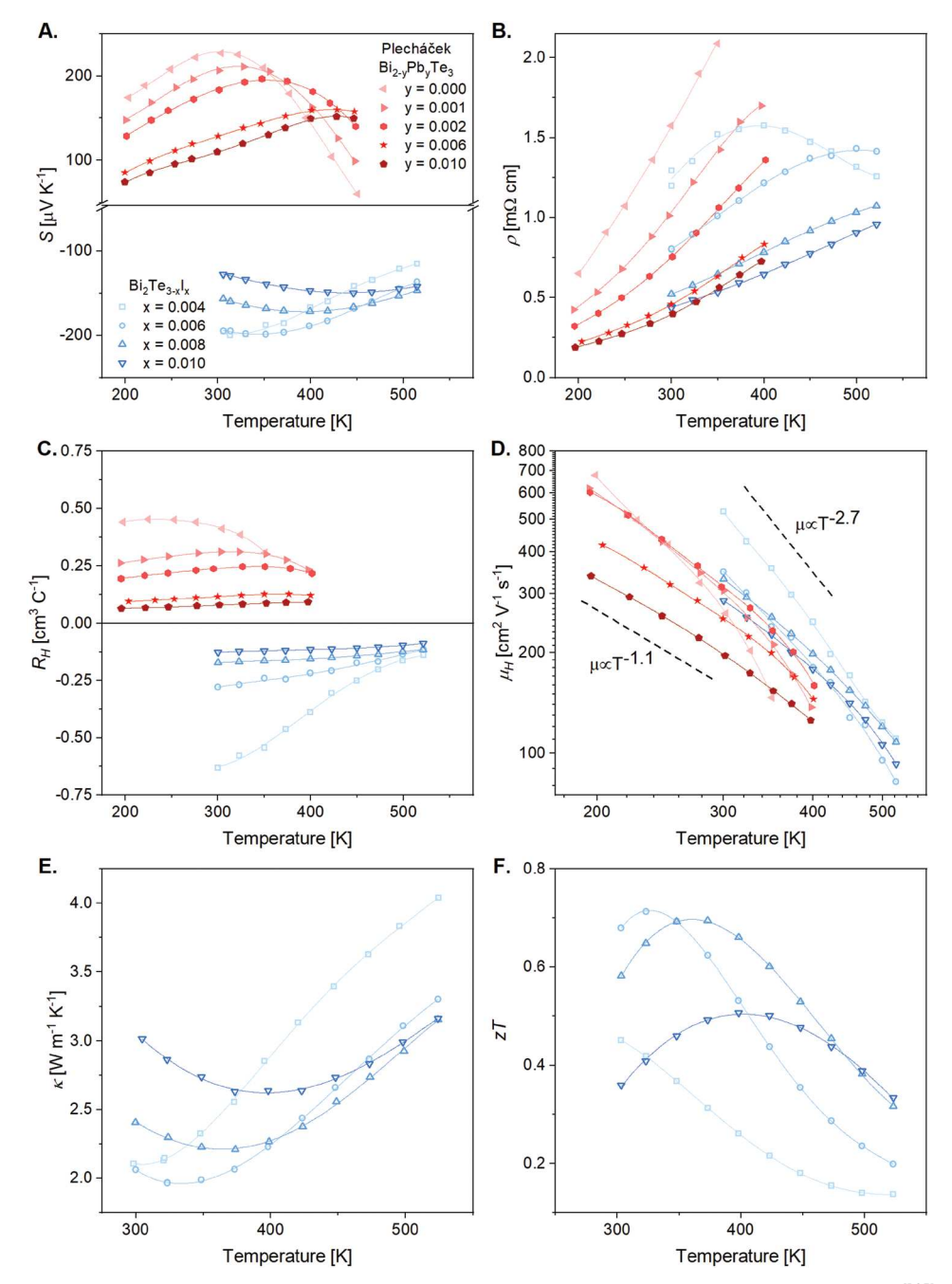


Figure 11. Thermal and electrical transport coefficient variation with temperature in I-doped n-type and Pb-doped p-type^[135] Bi_2Te_3 : (A) Seebeck coefficient, (B) Resistivity, (C) Hall coefficient, (D) Hall mobility, (E) Thermal conductivity, and (F) Figure of merit. Curves are only drawn as guides to the eye. The slopes in (D) are meant as references only and not to imply dependencies related to scattering mechanisms.

are consistently filled maintaining the $T^{-3/2}$ dependence in mobility.^[139]

Multiple studies have fit a mixed ionized and deformation potential scattering model to experimental data. [88,135,136,140] Full forms of the relaxation time can be found in Equations (S19)–(S23) in the Supporting Information , but a ratio is employed here to provide a better sense of relative magnitudes. The ratio of the prefactor for the relaxation times for ionized impurity, $\tau_{0,ii}$, to acoustic phonon, $\tau_{0,ac}$, scattering is proportional to material properties as shown in Equation (3). [141–143]

$$\frac{\tau_{0,ii}}{\tau_{0,ac}} \simeq \frac{m_b^{*2} \varepsilon^2 \Xi^2}{C_1} \tag{3}$$

where ε is the static dielectric constant. The larger this ratio, more deformation potential scattering would dominate charge transport with less influence due to ionized impurity scattering. This ratio for Bi₂Te₃ is 9×10^2 times larger than that for Si and 5×10^6 times larger than that for InSb illustrating why Bi₂Te₃ is relatively insensitive to impurities in the typical

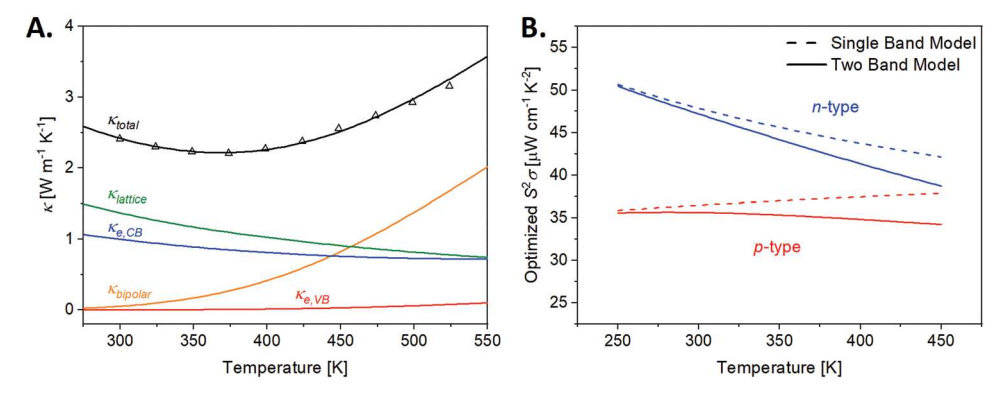


Figure 12. Two-band effective-mass model results of Bi_2Te_3 trends with temperature based on fits of the $Bi_2Te_{2.992}I_{0.008}$ sample. Breaking the total thermal conductivity into each contribution A) shows their relative magnitudes. The lattice thermal conductivity dominates at low temperatures and suggests potential benefits from microstructure engineering. At elevated temperatures, the bipolar thermal contribution is substantial, necessitating bandgap modification through alloying. The maximum power factor which can be achieved in Bi_2Te_3 assuming optimized doping for each temperature B) is also negatively impacted due to the subtracting effect of minority carriers on the thermopower.

range of operating temperatures (Table 1). [141,144–147] While the large dielectric constant of Bi₂Te₃ does play significant role in minimizing the effects of ionized impurities, but the effective masses, deformation potentials, and soft lattice are also important. Ionized impurity effects are observed in Bi₂Te₃, but only at low temperatures such as in the behavior Hall coefficient at temperatures 100 K and below. [135] Above this temperature, the $\approx T^{-3/2}$ mobility dependence for deformation potential scattering and $\approx T^{3/2}$ for ionized impurity scattering shifts the ratio toward deformation potential scattering. [141,143]

The thermal conductivity is strongly influenced by the effects of minority carriers due to the small bandgap as shown for the I-doped samples shown in Figure 11E. To examine the relative contributions of the lattice, electrical, and bipolar thermal conductivities to the total, we developed a simple two-band model with a CB and VB to fit the data from the x=0.008 n-type sample (Figure 12A). Details of this model and fits to the other transport measurements can be found in the Supporting Information. The bipolar contribution to thermal conductivity can be so significant near room temperature such that increasing the I-doping from x=0.004 to 0.006 reduces the total thermal conductivity even though the electrical resistivity also drops.

4. Alloying to Improve Thermoelectric Performance of Bi₂Te₃

The optimization of the performance of Bi $_2$ Te $_3$ is usually achieved by appropriate solid-solution alloying with Sb $_2$ Te $_3$, Sb $_2$ Se $_3$, Bi $_2$ Se $_3$, or Bi $_3$ Se $_3$ Se

Perhaps more importantly, alloys are typically chosen to tune the carrier concentration and thereby optimize the Fermi level. Even isoelectronic substitution of bismuth and tellurium can change the carrier density through the interaction of different point defects. This is because the substitution of Bi by Sb favors the formation of (Bi, Sb) on Te antisite defects leading to p-type conduction, while the substitution of Te by Se favors the formation of Se vacancies and the n-type conduction. [82] The atomic chemical potentials change continuously with the alloy composition and change the defect formation energies.^[85] The optimized composition for p-type material is near $(Sb_{0.75}Bi_{0.75})_2 Te_3^{[6,87,150]}$ where antisite Sb_{Te} defects provide \approx 7 \times 10¹⁹ holes cm⁻³ while typical n-type compositions containing about 10% Bi₂Se₃[32,79] show suppressed Bi_{Te} antisites and introduce Se vacancies that can make the material nearly intrinsic,[100] or nearly optimally doped for chalcogen rich material.^[151] Further doping with extrinsic impurities may be used for optimum tuning of the Fermi level. [6,79] The maximum zT may be tailored to lower or higher temperatures by fine tuning the charge carrier densities.^[78]

Besides its effect on the carrier concentration, the substitutional alloys of bismuth telluride display larger energy gaps than the binary itself as noted in (Figure 3), allowing for the minority carrier conduction to be suppressed up to higher temperatures.^[1] The detrimental effect of the minority carriers on the thermoelectric properties suggests that engineering the bandgap would be a viable strategy to improve the performance of Bi₂Te₃ as a thermoelectric generator. Above 325 K, when the bandgap is 5 k_BT the bipolar effect leads to a clear reduction in thermopower and increase in thermal conductivity^[1,32] that noticeably reduces zT.^[83,116] This issue is more pronounced in Bi₂Te₃ than PbTe due to the reduction of the energy gap with temperature for Bi_2Te_3 whereas E_{σ} conveniently increases with temperature for PbTe.[49] Thus, in order to extend the effectiveness to higher temperatures any optimization of Bi₂Te₃ should involve the increase of the energy gap which may be achieved by either doping or alloying and it is usually achieved through appropriate alloying. [29,116]

Mixtures with Bi_2Se_3 and Sb_2Te_3 both increase the bandgap from that of pure Bi_2Te_3 . In both alloy systems, the bandgap variation with composition does not follow Vegard's law but instead abruptly changes slope at an intermediate point

(Figure 3). This is due to the relative movement of multiple band edges with changing composition which also has consequences for the electronic transport behavior. The formation of the solid solutions is also accompanied by gradual changes of the band parameters such as effective masses and mobilities and even band convergence is observed. [6] In the Bi₂Te₃-Sb₂Te₃ system, a peak in hole weighted mobility occurs near (Bi_{0.25}Sb_{0.75})₂Te₃ and most p-type alloys are made near this composition. [6] In the Bi₂Te₃-Bi₂Se₃ system commonly used for n-type legs, the electron weighted mobility decreases monotonically with increasing selenide fraction. [139,148,152]

5. Use of on Bi₂Te₃ in Thermoelectric Devices

The chalcogenides of bismuth were some of the first materials tested for their thermoelectric effects by Johan Seebeck himself in 1822–23 when he examined the natural minerals Pilsenite $\approx\!Bi_4Te_3$ and bismuth glance $\approx\!Bi_2S_3$. In 1910, Haken reported data on the Bi-Te binary system which found that Bi_2Te_3 possessed a large Seebeck coefficient and could be made p- or n-type depending on if it was prepared Bi or Te-rich. [153]

Maria Telkes considered Bi₂Te₃ for use in some of the first generators reported in 1947.[154] The first experimental evidence that Bi₂Te₃ is a potential candidate for cooling applications dates back to 1954, when branches of p-type Bi₂Te₃ and n-type Bi were joined together to achieve a cooling effect of 26 °C below the ambient temperature. [155] In 1955, when both p-type and n-type Bi₂Te₃ were available, a higher cooling of 40 °C was attained, [156] which was further raised to 65 °C in 1958.[115] A significant optimization of the thermoelectric performance of bismuth telluride was achieved after adopting the ideas of Ioffe and Ioffe on semiconductor solid solutions.[157] Therefore, optimum alloys of Bi2Te3-Sb2Te3 and Bi₂Te₃-Bi₂Se₃ with low thermal conductivities were introduced for the first time in the late 1950s. [1,29,32,92,100,116,152,158,159] Since then. p-type Bi_{0.5}Sb_{1.5}Te₃ and n-type Bi₂Te_{2.7}Se_{0.3} constitute state-of-theart thermoelectric materials. They both show room temperature figure of merit ≈1, and can be used for both refrigeration and power generation.[32,79,116,160]

Today, commercially available single stage Peltier coolers based upon $\rm Bi_2Te_3$ can produce maximum temperature differences between 65 and 75 K with the hot side maintained at 300 K. $\rm ^{[161]}$ Multistage coolers can achieve higher temperature differences by avoiding thermoelectric compatibility problems. $\rm ^{[162]}$ By tuning the carrier concentration and zT of the low temperature stages the maximum temperature difference across a multistage unit could be increased by up to 9%. $\rm ^{[78]}$

Commercially available power generation modules operate near 13% of the Carnot efficiency. [163] As generators operate at elevated temperatures, suppressing bipolar effects and shifting zT is even more important. [164] Doping, alloying and material processing all effect thermoelectric transport properties and should lead to improved device performance as well. [14]

6. Conclusion

Bi₂Te₃ is a remarkably good thermoelectric material naturally having low lattice thermal conductivity and complex electronic

structure that effectively provides multiple low-mass conducting pockets. The structure also allows plentiful avenues for electronic doping and alloying without strongly detrimental effects to the mobility. By reviewing the crystal and electronic structure combined with a simple analysis of the transport parameters the basic strategies for improving the thermoelectric properties of $\rm Bi_2Te_3$ can be explained. Although zT measurements of this highly anisotropic material vary widely, the bandgap, weighted mobility, effective mass, lattice thermal conductivity follow physical trends that can be used to benchmark and explain improvements in the individual materials parameters, the thermoelectric quality factor and ultimately zT.

Above room temperature the thermoelectric performance benefits from increasing the bandgap through solid solution alloying with Sb₂Te₃ or Bi₂Se₃. Such alloys also induce band convergence which increases the density of states as well as reduce lattice thermal conductivity and ultimately quality factor.

The low minimum thermal conductivity calculated for $\mathrm{Bi}_2\mathrm{Te}_3$ suggests nanostructuring or microstructure engineering could make dramatic improvements in zT but this needs to be carefully weighed against increased scattering and unfavorable crystallographic orientation. High zT also requires appropriate doping which can be manipulated through extrinsic defects but often overwhelmed by intrinsic defects. Only by appreciating the complex interplay of effects can a true optimum performance be achieved.

7. Experimental Section

Electronic Structure Computation: The Bi_2Te_3 , Bi_2Se_3 , and Sb_2Te_3 compounds were taken in their trigonal crystal structure (space group R-3m) with experimental cell parameters from Materials Project^[165] as shown in the **Table 2**. The electronic band structures were calculated with density functional theory (DFT), using the Vienna Ab initio Simulation Package (VASP),^[166,167] using the Perdew–Burke–Ernzerhof (PBE)^[168] generalized gradient approximation (GGA) functional and adopting the projector augmented-wave (PAW)^[169,170] approach. SOI was included in all the calculations to obtain the complexity of the band structure, van der Waals interactions were not included.

A nonself consistent field (NSCF) calculation on a uniform grid of 670 irreducible k-points was performed in order to calculate the density of states, shown in Figure 2. On top of this calculation, an interpolation on a grid 50 times as dense, using BoltzTraP[171,172] software, was performed to obtain the Fermi surfaces shown in Figure 6 of the main manuscript. The band structure on the bisectrix plane for the three compounds, shown in Figure 5 of the main manuscript, were calculated using a NSCF calculation on a grid of 10 404 k-points.

The band structure on the high symmetry path Z- Γ -Z-f-a'(CBM)-a'(VBM)- Γ , shown in Figure 4, was calculated using 300 k-points along this path. This path was chosen to show all the band extrema found in the bisectrix plane plot (**Figure 13**). The atomic character of the bands is indicated by color.

Table 2. Experimental cell parameters used for electronic structure calculations.^[165]

Compound	$a = b = c [\mathring{A}]$	$\alpha = \beta = \gamma [^{\circ}]$	Volume [ų]
Bi ₂ Te ₃	10.468	24.164	168.933
Bi ₂ Se ₃	9.841	24.304	141.890
Sb ₂ Te ₃	10.284	23.851	156.217

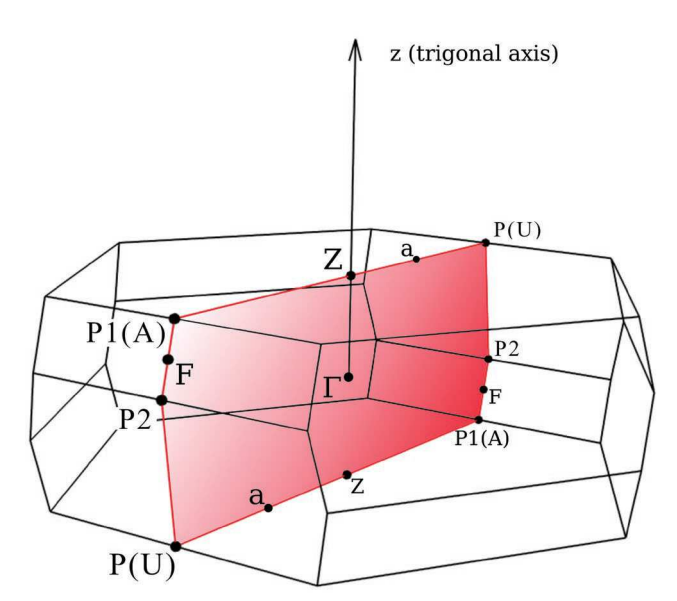


Figure 13. Brillouin zone for Bi_2Te_3 with the bisectrix mirror plane and key points in k-space indicated.

All data analyses (for example, band structure and Fermi surface plotting) were carried out using the pymatgen python package.^[173]

Synthesis of Iodine Doped Bi₂Te₃: Samples of iodine doped Bi₂Te₃ were synthesized from end member compositions of Bi₂Te_{3-x}I_x with x = 0 and 0.05. The end member compounds were synthesized from elements of Bi, Te, and the compound Bil₃ (Alfa Aesar, 99.999% purity metals basis). Stoichiometric amounts of each were loaded into carbon coated quartz ampoules, and evacuated to a pressure of $\approx 10^{-5}$ Torr. Due to the hygroscopic nature of Bil3, extra care was taken in the synthesis of the iodine doped end member and the starting elements and compounds were weighed out in an argon glove box. The sealed ampoules were placed in a vertical tube furnace, melted at 1173 K for 12 h, and water quenched. The resulting ingots were then blended in stoichiometric proportions in order to obtain samples of compositions $Bi_2Te_{3-x}I_x$ with x = 0.004, 0.006, 0.008, and 0.01. The blended ingots were placed in ampoules and then sealed under vacuum ($\approx 10^{-5}$ Torr), placed in a vertical tube furnace, melted at 1173 K for 12 h, and again water quenched. Ingots were then ground in an agate mortar and pestle for 20 min inside an Argon atmosphere to avoid oxygen contamination. The powders were placed in quartz ampoules, sealed under vacuum (≈10⁻⁵ Torr), placed in a resistive vertical tube furnace, melted at 1173 K for 5 min, and again water quenched. This step ensures a dense starting ingot for zone melting. Ingots at this step were of ≈80-90 mm in length. Directional solidification results in preferential orientation of the basal planes in $\mathrm{Bi}_{2}\mathrm{Te}_{3}.^{[174]}$ Zone melting was chosen as the processing technique due to the control of solute segregation and sample homogeneity. The ampoules were placed in a home built vertical zone melting furnace^[175] with a solidification rate of 2.7 mm h⁻¹ which resulted in oriented polycrystalline material. With great care one can achieve single crystals via zone melting, however, polycrystalline samples have the same transport behavior as single crystal Bi₂Te₃ provided the orientation is complete.^[32]

XRD Characterization of Samples: X-ray diffraction was conducted on samples of ${\rm Bi}_2{\rm Te}_3$ doped with iodine to ensure the crystallographic orientation was successful. Measurements were performed on parallelpiped samples utilizing a Philips PANalalytical X'Pert Pro with CuKa radiation, using a step size of 0.008° 2θ . The resulting data were refined using the Rietveld method with the FullProf program, starting with the atomic coordinates determined by Feutelais et al.[176] All reflections can be indexed to the space group *R-3m*, and no secondary reflections were observed.

Measurement of Transport Properties: The resistivity (ρ) and Hall effect measurements were done on parallepiped shape samples

 $(4.0 \times 1.5 \times 12.0 \text{ mm}^3)$ in a modified MMR technologies variable temperature Hall measurement system (VTHS) with a 1.0 T field up to 523 K. Measurements were done under dynamic vacuum and the 4-point method was used to measure resistivity. An additional contact was placed opposite one of the resistance voltage contacts to obtain Hall data without requiring a change in contact geometry. The Hall carrier concentration was calculated from the Hall coefficient from $R_{\rm H} = -1/en_{\rm H}$. The Hall mobility ($\mu_{\rm H}$) was determined from the measured resistivity and Hall carrier concentration using $\mu_{\rm H} = 1/n_{\rm H}ep$.

The Seebeck coefficient (S) was measured on pieces of the zone melted ingot at each end of the Hall parallelpiped to increase the confidence in the sample homogeneity. The measurements were performed under dynamic vacuum in a home-built system. A temperature gradient oscillated across the sample at 7.5 K while a constant average temperature was maintained at each point. Niobium-chromel thermocouples were used and resistive cartridge heaters maintain the temperature inside a BN cylinder. A 4-point in-line method was used that allowed for the temperature and voltage to be measured at the same point on the sample.

Measurements of the thermal diffusivity were performed using a Netsch LFA 457. The thermal conductivity was calculated based on $\kappa=DC_pd$ where D is the thermal diffusivity, C_p is the heat capacity, and d is the density. The temperature dependent heat capacity of Bi_2Te_3 reported by Shtern et al. was used. $^{[178]}$ The density was measured using the Archimedes method. The measurements were performed in an inert argon atmosphere, under a constant flow rate of 50–100 mL min $^{-1}$.

Optical Characterization: The optical measurements were performed at room temperature through diffuse reflectance infrared Fourier transform spectroscopy (DRIFTS), using a Nicolet 6700 FTIR spectrophotometer (Thermo Scientific) with an attached Praying Mantis Diffuse Reflectance accessory (Harrick), deuterated triglycerine sulfate (DTGS) detector and KBr beam splitter. The absorption coefficient was obtained using the Kubelka Munk function $F(R) = (a/s) = (1 - R)^2/2R$, where R is the fractional reflectance, a is the absorption coefficient as is the scattering coefficient. [179] In cases in which the particle size is greater than the wavelengths measured (2–20 mm), it is acceptable to assume the scattering coefficient to be independent of frequency.

Supporting Information

Supporting Information is available from the Wiley Online Library or from the author.

Acknowledgements

The authors would like to acknowledge EFRC Solid-State Solar-Thermal Energy Conversion Center (S3TEC), Grant DE-SC0001299, and funding from the National Science Foundation (DMREF-1729487). The authors also gratefully acknowledge thermoelectrics research at Northwestern University through the Center for Hierarchical Materials Design (CHiMaD).

Conflict of Interest

The authors declare no conflict of interest.

Keywords

bismuth telluride, electronic structures, thermoelectrics, transport modeling

Received: December 6, 2018 Revised: February 16, 2019 Published online: April 5, 2019

- [1] H. J. Goldsmid, Materials 2014, 7, 2577.
- [2] X. Hu, P. Jood, M. Ohta, M. Kunii, K. Nagase, H. Nishiate, M. G. Kanatzidis, A. Yamamoto, Energy Environ. Sci. 2016, 9, 517.
- [3] Q. Zhang, J. Liao, Y. Tang, M. Gu, C. Ming, P. Qiu, S. Bai, X. Shi, C. Uher, L. Chen, Energy Environ. Sci. 2017, 10, 956.
- [4] J. P. Heremans, R. J. Cava, N. Samarth, Nat. Rev. Mater. 2017, 2, 17049
- [5] J. P. Heremans, B. Wiendlocha, in Materials Aspect of Thermoelectricity (Ed: C. Uher), CRC Press, Boca Raton, FL 2016, pp. 39–94.
- [6] H.-S. Kim, N. A. Heinz, Z. M. Gibbs, Y. Tang, S. D. Kang, G. J. Snyder, *Mater. Today* 2017, 20, 452.
- [7] Y. Pei, H. Wang, G. J. Snyder, Adv. Mater. 2012, 24, 6125.
- [8] B. Wiendlocha, J. Electron. Mater. 2016, 45, 3515.
- [9] C. M. Jaworski, V. Kulbachinskii, J. P. Heremans, *Phys. Rev. B* 2009, 80, 233201.
- [10] B. Poudel, Q. Hao, Y. Ma, Y. Lan, A. Minnich, B. Yu, X. Yan, D. Wang, A. Muto, D. Vashaee, X. Chen, J. Liu, M. S. Dresselhaus, G. Chen, Z. Ren, *Science* 2008, 320, 634.
- [11] S. I. Kim, K. H. Lee, H. A. Mun, H.-S. Kim, S. W. Hwang, J. W. Roh, D. J. Yang, W. H. Shin, X. S. Li, Y. H. Lee, G. J. Snyder, S. W. Kim, *Science* 2015, 348, 109.
- [12] Y. Zheng, Q. Zhang, X. Su, H. Xie, S. Shu, T. Chen, G. Tan, Y. Yan, X. Tang, C. Uher, G. J. Snyder, Adv. Energy Mater. 2015, 5, 1401391.
- [13] Y. Pan, U. Aydemir, J. A. Grovogui, I. T. Witting, R. Hanus, Y. Xu, J. Wu, C.-F. Wu, F.-H. Sun, H.-L. Zhuang, J.-F. Dong, J.-F. Li, V. P. Dravid, G. J. Snyder, Adv. Mater. 2018, 30, 1802016.
- [14] S. Wang, W. Xie, H. Li, X. Tang, Intermetallics 2011, 19, 1024.
- [15] A. Purkayastha, Q. Yan, M. S. Raghuveer, D. D. Gandhi, H. Li, Z. W. Liu, R. V. Ramanujan, T. Borca-Tasciuc, G. Ramanath, Adv. Mater. 2008, 20, 2679.
- [16] A. Purkayastha, S. Kim, D. D. Gandhi, P. G. Ganesan, T. Borca-Tasciuc, G. Ramanath, Adv. Mater. 2006, 18, 2958.
- [17] A. Purkayastha, F. Lupo, S. Kim, T. Borca-Tasciuc, G. Ramanath, Adv. Mater. 2006, 18, 496.
- [18] X. B. Zhao, X. H. Ji, Y. H. Zhang, T. J. Zhu, J. P. Tu, X. B. Zhang, Appl. Phys. Lett. 2005, 86, 062111.
- [19] L. Hu, H. Gao, X. Liu, H. Xie, J. Shen, T. Zhu, X. Zhao, J. Mater. Chem. 2012, 22, 16484.
- [20] L. P. Hu, X. H. Liu, H. H. Xie, J. J. Shen, T. J. Zhu, X. B. Zhao, Acta Mater. 2012, 60, 4431.
- [21] M. Saleemi, M. S. Toprak, S. Li, M. Johnsson, M. Muhammed, J. Mater. Chem. 2012, 22, 725.
- [22] Y. Lan, B. Poudel, Y. Ma, D. Wang, M. S. Dresselhaus, G. Chen, Z. Ren, Nano Lett. 2009, 9, 1419.
- [23] P. W. Lange, Die Naturwissensch. 1939, 27, 133.
- [24] S. Lee, K. Esfarjani, T. Luo, J. Zhou, Z. Tian, G. Chen, Nat. Commun. 2014, 5, 3525.
- [25] W. G. Zeier, A. Zevalkink, Z. M. Gibbs, G. Hautier, M. G. Kanatzidis, G. J. Snyder, Angew. Chem., Int. Ed. 2016, 55, 6826.
- [26] G. Li, U. Aydemir, S. I. Morozov, M. Wood, Q. An, P. Zhai, Q. Zhang, W. A. Goddard, G. J. Snyder, *Phys. Rev. Lett.* 2017, 119, 085501.
- [27] J. R. Drabble, C. H. L. Goodman, J. Phys. Chem. Solids 1958, 5, 142.
- [28] S. Scherrer, H. Scherrer, in CRC Handbook of Thermoelectrics (Ed: D. M. Rowe), CRC Press, Boca Raton, FL 1995.
- [29] H. J. Goldsmid, J. Appl. Phys. 1961, 32, 2198.
- [30] H. Kaibe, Y. Tanaka, M. Sakata, I. Nishida, J. Phys. Chem. Solids 1989, 50, 945.
- [31] B. M. Goltsman, B. A. Kudinov, I. A. Smirnov, Thermoelectric Semiconductor Materials Based on Bi₂Te₃, Defense Technical Information Center, Ft. Belvoir, VA 1973.
- [32] H. J. Goldsmid, Introduction to Thermoelectricity, Springer, Berlin, 2016.

- [33] M. Situmorang, H. J. Goldsmid, Physica Status Solidi B 1986, 134, K83.
- [34] H. J. Goldsmid, F. A. Underwood, Adv. Energy Convers. 1968, 7, 297
- [35] S. J. Youn, A. J. Freeman, Phys. Rev. B 2001, 63, 085112.
- [36] B. Y. Yavorsky, N. F. Hinsche, I. Mertig, P. Zahn, Phys. Rev. B 2011, 84, 165208.
- [37] S. K. Mishra, S. Satpathy, O. Jepsen, J. Phys.: Condens. Matter 1997, 9, 461.
- [38] B.-L. Huang, M. Kaviany, Phys. Rev. B 2008, 77, 1.
- [39] H. A. Ashworth, J. A. Rayne, R. W. Ure, Phys. Rev. B 1971, 3, 2646.
- [40] H. Köhler, Phys. Status Solidi B 1976, 74, 591.
- [41] H. Köhler, Phys. Status Solidi B 1976, 73, 95.
- [42] H. Köhler, G. Landwehr, Phys. Status Solidi B 1971, 45, K109.
- [43] B. Schröder, A. von Middendorff, H. Köhler, G. Landwehr, Phys. Status Solidi B 1973, 59, 561.
- [44] D. I. Bilc, S. D. Mahanti, M. G. Kanatzidis, Phys. Rev. B 2006, 74, 125202.
- [45] P. Larson, S. Mahanti, M. G. Kanatzidis, Phys. Rev. B 2000, 61, 8162.
- [46] P. Larson, Phys. Rev. B 2003, 68, 155121.
- [47] P. Pecheur, G. Toussaint, Phys. Lett. A 1989, 135, 223.
- [48] I. G. Austin, Proc. Phys. Soc. 1958, 72, 545.
- [49] Z. M. Gibbs, H. Kim, H. Wang, R. L. White, F. Drymiotis, M. Kaviany, G. Jeffrey Snyder, Appl. Phys. Lett. 2013, 103, 262109.
- [50] H. Shi, D. Parker, M. H. Du, D. J. Singh, Phys. Rev. Appl. 2015, 3, 1.
- [51] G. A. Thomas, D. H. Rapkine, R. B. Van Dover, L. F. Mattheiss, W. A. Sunder, L. F. Schneemeyer, J. V. Waszczak, *Phys. Rev. B* 1992, 46, 1553.
- [52] Z. Ren, A. A. Taskin, S. Sasaki, K. Segawa, Y. Ando, Phys. Rev. B 2011, 84, 165311.
- [53] Z. Ren, A. A. Taskin, S. Sasaki, K. Segawa, Y. Ando, Phys. Rev. B 2010, 82, 241306.
- [54] Y. Xia, D. Qian, D. Hsieh, L. Wray, A. Pal, H. Lin, A. Bansil, D. Grauer, Y. S. Hor, R. J. Cava, M. Z. Hasan, *Nat. Phys.* 2009, 5, 398.
- [55] H. Zhang, C.-X. Liu, X.-L. Qi, X. Dai, Z. Fang, S.-C. Zhang, Nat. Phys. 2009, 5, 438.
- [56] Y. L. Chen, J. G. Analytis, J.-H. Chu, Z. K. Liu, S.-K. Mo, X. L. Qi, H. J. Zhang, D. H. Lu, X. Dai, Z. Fang, S. C. Zhang, I. R. Fisher, Z. Hussain, Z.-X. Shen, *Science*. 2009, 325, 178.
- [57] A. Soumyanarayanan, N. Reyren, A. Fert, C. Panagopoulos, *Nature* 2016, 539, 509.
- [58] M. Z. Hasan, C. L. Kane, Rev. Mod. Phys. 2010, 82, 3045.
- [59] L. L. Wang, M. Huang, S. Thimmaiah, A. Alam, S. L. Bud'Ko, A. Kaminski, T. A. Lograsso, P. Canfield, D. D. Johnson, *Phys. Rev. B* 2013, 87, 1.
- [60] D. O. Scanlon, P. D. C. King, R. P. Singh, A. De La Torre, S. M. Walker, G. Balakrishnan, F. Baumberger, C. R. A. Catlow, Adv. Mater. 2012, 24, 2154.
- [61] S. Jia, H. Ji, E. Climent-Pascual, M. K. Fuccillo, M. E. Charles, J. Xiong, N. P. Ong, R. J. Cava, Phys. Rev. B 2011, 84, 1.
- [62] G. Wang, T. Cagin, Phys. Rev. B 2007, 76, 075201.
- [63] D. L. Greenaway, G. Harbeke, J. Phys. Chem. Solids 1965, 26, 1585.
- [64] Z. M. Gibbs, A. LaLonde, G. J. Snyder, New J. Phys. 2013, 15, 075020.
- [65] M. Kim, A. J. Freeman, C. B. Geller, Phys. Rev. B 2005, 72, 2.
- [66] J. M. Crowley, J. Tahir-Kheli, W. A. Goddard, J. Phys. Chem. Lett. 2015, 6, 3792.
- [67] T. J. Scheidemantel, C. Ambrosch-Draxl, T. Thonhauser, J. V. Badding, J. O. Sofo, Phys. Rev. B 2003, 68, 125210.
- [68] I. A. Nechaev, R. C. Hatch, M. Bianchi, D. Guan, C. Friedrich, I. Aguilera, J. L. Mi, B. B. Iversen, S. Blügel, P. Hofmann, E. V. Chulkov, *Phys. Rev. B* 2013, 87, 121111.



- [69] J. R. Drabble, Proc. Phys. Soc. 1958, 72, 380.
- [70] J. R. Drabble, R. D. Groves, R. Wolfe, Proc. Phys. Soc. 1958, 71, 430.
- [71] L. R. Testardi, P. J. Stiles, E. Burstein, Solid State Commun. 1963, 1, 28.
- [72] R. B. Mallinson, J. A. Rayne, R. W. Ure, Phys. Lett. A 1967, 24, 713.
- [73] R. B. Mallinson, J. A. Rayne, R. W. Ure, Phys. Rev. 1968, 175, 1049.
- [74] H. J. Noh, H. Koh, S. J. Oh, J. H. Park, H. D. Kim, J. D. Rameau, T. Valla, T. E. Kidd, P. D. Johnson, Y. Hu, Q. Li, *Europhys. Lett.* 2008, 81, 57006.
- [75] V. A. Greanya, W. C. Tonjes, R. Liu, C. G. Olson, D. Y. Chung, M. G. Kanatzidis, *Phys. Rev. B* 2000, 62, 16425.
- [76] H. Köhler, W. Haigis, A. von Middendorff, Phys. Status Solidi B 1976, 78, 637.
- [77] Y. Pei, X. Shi, A. LaLonde, H. Wang, L. Chen, G. J. Snyder, Nature 2011, 473, 66.
- [78] V. A. Kutasov, L. N. Lukyanova, M. V. Vedernikov, in *Thermoelectrics Handbook: Macro to Nano* (Ed: D. M. Rowe), CRC Press, Boca Raton, FL 2005, pp. 1–18.
- [79] L. V. Prokofieva, D. A. Pshenay-Severin, P. P. Konstantinov, A. A. Shabaldin, Semiconductors 2009, 43, 973.
- [80] F. Hao, P. Qiu, Y. Tang, S. Bai, T. Xin, H. Chu, Q. Zhang, P. Lu, T. Zhang, D. Ren, J. Chen, X. Shi, L. Chen, *Energy Environ. Sci.* 2016, 9, 3120.
- [81] W.-S. Liu, Q. Zhang, Y. Lan, S. Chen, X. Yan, Q. Zhang, H. Wang, D. Wang, G. Chen, Z. Ren, Adv. Energy Mater. 2011, 1, 577.
- [82] T. Zhu, L. Hu, X. Zhao, J. He, Adv. Sci. 2016, 3, 1600004.
- [83] C. B. Satterthwaite, R. W. Ure, Phys. Rev. 1957, 108, 1164.
- [84] J.-P. Fleurial, L. Gailliard, R. Triboulet, H. Scherrer, S. Scherrer, J. Phys. Chem. Solids 1988, 49, 1237.
- [85] S. Ohno, K. Imasato, S. Anand, H. Tamaki, S. D. Kang, P. Gorai, H. K. Sato, E. S. Toberer, T. Kanno, G. J. Snyder, *Joule* 2018, 2, 141.
- [86] G. R. Miller, C.-Y. Li, J. Phys. Chem. Solids 1965, 26, 173.
- [87] H. Scherrer, S. Scherrer, in Thermoelectrics Handbook: Macro to Nano (Ed: D. M. Rowe), CRC Press, Boca Raton, FL 2005, pp. 27-1–27-19.
- [88] J.-P. Fleurial, L. Gailliard, R. Triboulet, H. Scherrer, S. Scherrer, J. Phys. Chem. Solids 1988, 49, 1249.
- [89] N. Fuschillo, J. N. Bierly, F. J. Donahoe, J. Phys. Chem. Solids 1959, 8, 430.
- [90] T. C. Chasapis, D. Koumoulis, B. Leung, N. P. Calta, S.-H. Lo, V. P. Dravid, L.-S. Bouchard, M. G. Kanatzidis, APL Mater. 2015, 3, 083601.
- [91] H. Wang, X. Cao, Y. Takagiwa, G. J. Snyder, Mater. Horiz. 2015, 2, 323.
- [92] W. M. Yim, F. D. Rosi, Solid-State Electron. 1972, 15, 1121.
- [93] R. J. Cava, H. Ji, M. K. Fuccillo, Q. D. Gibson, Y. S. Hor, J. Mater. Chem. C 2013, 1, 3176.
- [94] J. Bludská, I. Jakubec, Č. Drašar, P. Lošťák, J. Horák, *Philos. Mag.* 2007, 87, 325.
- [95] J. Horák, L. Tichy, P. Lošťák, A. Vasko, Cryst. Lattice Defects 1976, 6, 233.
- [96] P. Lošt'ák, Č. Drašar, J. Horák, Z. Zhou, J. S. Dyck, C. Uher, J. Phys. Chem. Solids 2006, 67, 1457.
- [97] T. Plecháček, J. Navrátil, J. Horák, D. Bachan, A. Krejčová, P. Lošťák, Solid State Ionics 2007, 177, 3513.
- [98] J. Navrátil, I. Klichová, S. Karamazov, J. Šrámková, J. Horák, J. Solid State Chem. 1998, 140, 29.
- [99] V. I. Fistul, Heavily Doped Semiconductors, Plenum Press, New York 1969.
- [100] U. Birkholz, Z. Naturforsch. 1958, 13a, 780.
- [101] M. K. Zhitinskaya, S. A. Nemov, T. E. Svechnikova, *Phys. Solid State* 1998, 40, 1297.

- [102] G. T. Alekseeva, P. P. Konstantinov, V. A. Kutasov, L. N. Luk'yanova, Y. I. Ravich, *Phys. Solid State* **1996**, *38*, 1639.
- [103] S. K. Kushwaha, Q. D. Gibson, J. Xiong, I. Pletikosic, A. P. Weber, A. V. Fedorov, N. P. Ong, T. Valla, R. J. Cava, J. Appl. Phys. 2014, 143708, 115.
- [104] S. K. Kushwaha, I. Pletikosić, T. Liang, A. Gyenis, S. H. Lapidus, Y. Tian, H. Zhao, K. S. Burch, J. Lin, W. Wang, H. Ji, A. V. Fedorov, A. Yazdani, N. P. Ong, T. Valla, R. J. Cava, *Nat. Commun.* 2016, 7, 11456.
- [105] L. Hu, T. Zhu, X. Liu, X. Zhao, Adv. Funct. Mater. 2014, 24, 5211.
- [106] J. Navrátil, Z. Starý, T. Plecháček, Mater. Res. Bull. 1996, 31, 1559.
- [107] C.-H. Kuo, C.-S. Hwang, M.-S. Jeng, W.-S. Su, Y.-W. Chou, J.-R. Ku, J. Alloys Compd. 2010, 496, 687.
- [108] Y. Pan, T.-R. Wei, C.-F. Wu, J.-F. Li, J. Mater. Chem. C 2015, 3, 10583.
- [109] B. Deb, Y. Isoda, O. Caballero-Calero, P. Díaz-Chao, M. S. Martín-González, Y. Shinohara, *Mater. Trans.* 2012, 53, 1481.
- [110] J. Jiang, L. Chen, S. Bai, Q. Yao, Q. Wang, Mater. Sci. Eng., B 2005, 117, 334.
- [111] T. S. Oh, D. B. Hyun, N. V. Kolomoets, Scr. Mater. 2000, 42, 849.
- [112] J.-F. Li, J. Liu, Phys. Status Solidi A 2006, 203, 3768.
- [113] H. Wang, Y. Pei, A. D. LaLonde, G. J. Snyder, in *Thermoelectric Nanomaterials* (Eds: T. Koumoto, K. Mori), Springer, Berlin 2013, pp. 3–32.
- [114] S. D. Kang, G. J. Snyder, arXiv:1710.06896 [cond-mat.mtrl-sci], http://arxiv.org/abs/1710.06896 (accessed October 2017).
- [115] H. J. Goldsmid, A. R. Sheard, D. A. Wright, Br. J. Appl. Phys. 1958, 9, 365.
- [116] H. J. Goldsmid, Thermoelectric Refrigeration, Plenum Press, New York 1964.
- [117] R. P. Chasmar, R. Stratton, J. Electron. Control 1959, 7, 52.
- [118] R. Deng, X. Su, Z. Zheng, W. Liu, Y. Yan, Q. Zhang, V. P. Dravid, C. Uher, M. G. Kanatzidis, X. Tang, Sci. Adv. 2018, 4, eaar5606.
- [119] E. H. Putley, J. Phys. C: Solid State Phys. 1975, 8, 1837.
- [120] G. N. Gordiakova, G. V. Kokosh, S. S. Sinani, Sov. Phys.-Tech. Phys. 1958, 3, 1.
- [121] S. Shigetomi, S. Mori, J. Phys. Soc. Jpn. 1956, 11, 915.
- [122] J. Li, X. Zhang, Z. Chen, S. Lin, W. Li, J. Shen, I. T. Witting, A. Faghaninia, Y. Chen, A. Jain, L. Chen, G. J. Snyder, Y. Pei, *Joule* 2018, 2, 976.
- [123] Y. Tang, Z. M. Gibbs, L. A. Agapito, G. Li, H.-S. Kim, M. B. Nardelli, S. Curtarolo, G. J. Snyder, *Nat. Mater.* 2015, 14, 1223.
- [124] S. Wang, G. Tan, W. Xie, G. Zheng, H. Li, J. Yang, X. Tang, J. Mater. Chem. 2012, 22, 20943.
- [125] R. M. Vlasova, L. S. Stilbans, Zh. Tekh. Fiz. 1955, 25, 569.
- [126] T. C. Harman, B. Paris, S. E. Miller, H. L. Goering, J. Phys. Chem. Solids 1957, 2, 181.
- [127] J. R. Drabble, R. Wolfe, Proc. Phys. Soc. Sect. B 1956, 69, 1101.
- [128] J. O. Jenkins, J. A. Rayne, R. W. Ure, Phys. Rev. B 1972, 5, 3171.
- [129] M. T. Agne, R. Hanus, G. J. Snyder, Energy Environ. Sci. 2018, 11, 609.
- [130] D. G. Cahill, S. K. Watson, R. O. Pohl, Phys. Rev. B 1992, 46, 6131.
- [131] A. M. Dehkordi, M. Zebarjadi, J. He, T. M. Tritt, *Mater. Sci. Eng., R* 2015, 97, 1.
- [132] T. Plecháček, J. Navrátil, J. Horák, P. Lošťák, Philos. Mag. 2004, 84, 2217.
- [133] H. J. Goldsmid, J. W. Sharp, J. Electron. Mater. 1999, 28, 869.
- [134] Z. M. Gibbs, H.-S. Kim, H. Wang, G. J. Snyder, Appl. Phys. Lett. 2015, 106, 022112.
- [135] B. A. Efimova, I. Y. Korenblum, V. I. Novikov, A. G. Ostroumov, Sov. Phys.-Solid State 1962, 3, 2004.

- [136] M. N. Vinogradova, O. A. Golikova, B. A. Efimova, V. A. Kutasov, T. S. Stavitskaya, L. S. Stil'bans, L. M. Sysoeva, Sov. Phys.-Solid State 1960, 1, 1224.
- [137] R. Mansfield, W. Williams, Proc. Phys. Soc. 1958, 72, 733.
- [138] H.-W. Jeon, H.-P. Ha, D.-B. Hyun, J.-D. Shim, *J. Phys. Chem. Solids* **1991**, *52*, 579.
- [139] I. T. Witting, F. Ricci, T. Chasapis, G. Hautier, G. J. Snyder, unpublished.
- [140] B. A. Efimova, E. V. Kel'man, L. S. Stil'bans, Sov. Phys.-Solid State 1962, 4, 108.
- [141] J. Bardeen, W. Shockley, Phys. Rev. 1950, 80, 72.
- [142] E. Conwell, V. F. Weisskopf, Phys. Rev. 1950, 77, 388.
- [143] H. Brooks, in Advances in Electronics and Electron Physics, Vol. 7 (Ed: L. Marton), Academic Press, Inc., New York 1955, pp. 85–182.
- [144] O. Madelung, U. Rössler, in Non-Tetrahedrally Bonded Elements and Binary Compounds I (Ed: M. Schulz), Springer-Verlag, Berlin 1998.
- [145] J. Jenkins, J. Rayne, R. Ure, Phys. Rev. B 1972, 6, 1609.
- [146] D. L. Rode, Phys. Rev. B 1971, 3, 3287.
- [147] K. M. Demchuk, I. M. Tsidilkovskii, Phys. Status Solidi 1977, 82, 59.
- [148] W. Liu, K. C. Lukas, K. McEnaney, S. Lee, Q. Zhang, C. P. Opeil, G. Chen, Z. Ren, *Energy Environ. Sci.* 2013, 6, 552.
- [149] H. Wang, A. D. LaLonde, Y. Pei, G. J. Snyder, Adv. Funct. Mater. 2013, 23, 1586.
- [150] M. Stordeur, Phys. Status Solidi B 1990, 161, 831.
- [151] M. Carle, P. Pierrat, C. Lahalle-Gravier, S. Scherrer, H. Scherrer, J. Phys. Chem. Solids 1995, 56, 201.
- [152] C. H. Champness, W. B. Muir, P. T. Chiang, Can. J. Phys. 1967, 45, 3611.
- [153] W. Haken, Ann. Phys. 1910, 337, 291.
- [154] M. Telkes, J. Appl. Phys. 1947, 18, 1116.
- [155] H. J. Goldsmid, R. W. Douglas, Br. J. Appl. Phys. 1954, 5, 386.
- [156] H. J. Goldsmid, J. Electron. Control 1955, 1, 218.
- [157] A. V. Ioffe, A. F. Ioffe, Sov. Phys.-Solid State 1960, 2, 719.
- [158] F. D. Rosi, B. Abeles, R. V. Jensen, J. Phys. Chem. Solids 1959, 10, 191.
- [159] C. H. Champness, P. T. Chiang, P. Parekh, Can. J. Phys. 1965, 43, 653.
- [160] P. P. Konstantinov, L. V. Prokofieva, M. I. Fedorov, D. A. Pshenay-Severin, Y. I. Ravich, V. V. Kompaniets, V. A. Chistyakov, *Semiconductors* 2005, 39, 1023.
- [161] D. Zhao, G. Tan, Appl. Therm. Eng. 2014, 66, 15.
- [162] G. J. Snyder, E. S. Toberer, R. Khanna, W. Seifert, Phys. Rev. B 2012, 86, 045202.
- [163] T. Kuroki, K. Kabeya, K. Makino, T. Kajihara, H. Kaibe, H. Hachiuma, H. Matsuno, A. Fujibayashi, J. Electron. Mater. 2014, 43, 2405.
- [164] F. Hao, P. Qiu, Y. Tang, S. Bai, T. Xing, H.-S. Chu, Q. Zhang, P. Lu, T. Zhang, D. Ren, J. Chen, X. Shi, L. Chen, *Energy Environ. Sci.* 2016, 9, 3120.
- [165] A. Jain, S. P. Ong, G. Hautier, W. Chen, W. D. Richards, S. Dacek, S. Cholia, D. Gunter, D. Skinner, G. Ceder, K. A. Persson, APL Mater. 2013, 1, 011002.
- [166] G. Kresse, J. Hafner, Phys. Rev. B 1993, 47, 558.
- [167] G. Kresse, J. Furthmüller, Phys. Rev. B 1996, 54, 11169.
- [168] J. P. Perdew, K. Burke, M. Ernzerhof, Phys. Rev. Lett. 1996, 77, 3865.
- [169] P. E. Blöchl, Phys. Rev. B 1994, 50, 17953.
- [170] G. Kresse, D. Joubert, Phys. Rev. B 1999, 59, 1758.
- [171] G. K. H. Madsen, D. J. Singh, Comput. Phys. Commun. 2006, 175, 67.
- [172] G. K. H. Madsen, J. Carrete, M. J. Verstraete, Comput. Phys. Commun. 2018, 231, 140.

- [173] S. P. Ong, W. D. Richards, A. Jain, G. Hautier, M. Kocher, S. Cholia, D. Gunter, V. L. Chevrier, K. A. Persson, G. Ceder, Comput. Mater. Sci. 2013, 68, 314.
- [174] C. H. Champness, P. T. Chiang, K. Grabowski, W. B. Muir, J. Appl. Phys. 1968, 39, 4177.
- [175] T. Ikeda, N. J. Marolf, G. J. Snyder, Cryst. Growth Des. 2011, 11, 4183.
- [176] Y. Feutelais, B. Legendre, N. Rodier, V. Agafonov, *Mater. Res. Bull.* 1993. 28, 591.
- [177] S. Iwanaga, E. S. Toberer, A. LaLonde, G. J. Snyder, Rev. Sci. Instrum. 2011, 82, 063905.
- [178] Y. I. Shtern, A. S. Malkova, A. S. Pashinkin, V. A. Fedorov, Inorg. Mater. 2008, 44, 1057.
- [179] P. Kubelka, F. Munk, Z. Tech. Phys. 1931, 12, 593.
- [180] A. Walsh, D. J. Payne, R. G. Egdell, G. W. Watson, Chem. Soc. Rev. 2011, 40, 4455.
- [181] R. Sehr, L. R. Testardi, J. Phys. Chem. Solids 1962, 23, 1219.
- [182] M. C. Peters, I. T. Witting, G. J. Snyder, P. W. Voorhees, unpublished.
- [183] G. J. Tan, S. Y. Wang, Y. G. Yan, H. Li, X. F. Tang, J. Electron. Mater. 2012, 41, 1147.
- [184] K. A. Borup, J. de Boor, H. Wang, F. Drymiotis, F. Gascoin, X. Shi, L. Chen, M. I. Fedorov, E. Müller, B. B. Iversen, G. J. Snyder, Energy Environ. Sci. 2015, 8, 423.
- [185] L. Hu, H. Wu, T. Zhu, C. Fu, J. He, P. Ying, X. Zhao, Adv. Energy Mater. 2015, 5, 1500411.
- [186] H. Tamaki, H. K. Sato, T. Kanno, Adv. Mater. 2016, 28, 10182.
- [187] A. D. LaLonde, Y. Pei, G. J. Snyder, Energy Environ. Sci. 2011, 4, 2090.
- [188] S. K. Bux, M. T. Yeung, E. S. Toberer, G. J. Snyder, R. B. Kaner, J.-P. Fleurial, J. Mater. Chem. 2011, 21, 12259.
- [189] G. Tan, F. Shi, S. Hao, L.-D. Zhao, H. Chi, X. Zhang, C. Uher, C. Wolverton, V. P. Dravid, M. G. Kanatzidis, Nat. Commun. 2016, 7, 12167.
- [190] E. A. Skrabek, D. S. Trimmer, in CRC Handbook of Thermoelectrics (Ed: D. M. Rowe), CRC Press, Boca Raton, FL 1995, pp. 267–275.
- [191] S. R. Culp, S. J. Poon, N. Hickman, T. M. Tritt, J. Blumm, Appl. Phys. Lett. 2006, 88, 042106.
- [192] J. Navrátil, P. Lošt'ák, J. Horák, Cryst. Res. Technol. 1991, 26, 675.
- [193] P. Lošťák, Č. Drašar, D. Bachan, L. Beneš, A. Krejčová, Radiat. Eff. Defects Solids 2010, 165, 211.
- [194] W. Richter, C. R. Becker, Phys. Status Solidi B 1977, 84, 619.
- [195] M. Stordeur, M. Stölzer, H. Sobotta, V. Riede, *Phys. Status Solidi B* 1988, 150, 165.
- [196] C.-Y. Lee, Phys. Rev. B 1987, 35, 4511.
- [197] H. Wang, J. Wang, X. Cao, G. J. Snyder, J. Mater. Chem. A 2014, 2, 3169.
- [198] H. Wang, Y. Pei, A. D. LaLonde, G. J. Snyder, Proc. Natl. Acad. Sci. USA 2012, 109, 9705.
- [199] H. Wang, Y. Pei, A. D. Lalonde, G. J. Snyder, *Adv. Mater.* **2011**, *23*, 1366.
- [200] Y. Pei, A. LaLonde, S. Iwanaga, G. J. Snyder, *Energy Environ. Sci.* 2011, 4, 2085.
- [201] Z. Chen, B. Ge, W. Li, S. Lin, J. Shen, Y. Chang, R. Hanus, G. J. Snyder, Y. Pei, *Nat. Commun.* 2017, 8, 13828.
- [202] K. M. Rabe, J. D. Joannopoulos, Phys. Rev. B 1987, 36, 6631.
- [203] G. Busch, U. Winkler, *Physica* **1954**, *20*, 1067.
- [204] J. Tani, H. Kido, Phys. B 2005, 364, 218.
- [205] H. Mizoguchi, Y. Muraba, D. C. Fredrickson, S. Matsuishi, T. Kamiya, H. Hosono, Angew. Chem. 2017, 129, 10269.
- [206] W. B. Whitten, P. L. Chung, G. C. Danielson, J. Phys. Chem. Solids 1965. 26, 49.
- [207] K. Imasato, S. D. Kang, S. Ohno, G. J. Snyder, *Mater. Horiz.* 2018, 5, 59.



www.advancedsciencenews.com

Adv. Electron. Mater. 2019, 5, 1800904

ADVANCED
ELECTRONIC
MATERIALS

- [208] D. W. Zhou, J. S. Liu, S. H. Xu, P. Peng, Phys. B 2010, 405, 2863.
- [209] V. Ponnambalam, D. T. Morelli, J. Electron. Mater. 2013, 42, 1307.
- [210] A. C. Kraemer, C. A. Perottoni, J. A. H. da Jornada, Solid State Commun. 2005, 133, 173.
- [211] T. Caillat, A. Borshchevsky, J.-P. Fleurial, J. Appl. Phys. 1996, 80, 4442.
- [212] J. Schmitt, Z. M. Gibbs, G. J. Snyder, C. Felser, *Mater. Horiz.* **2015**,
- [213] C. Yu, H. Xie, C. Fu, T. Zhu, X. Zhao, J. Mater. Res. 2012, 27, 2457.
- [214] S. Öğüt, K. M. Rabe, Phys. Rev. B 1995, 51, 10443.
- [215] D. F. Zou, S. H. Xie, Y. Y. Liu, J. G. Lin, J. Y. Li, J. Appl. Phys. **2013**, 113, 193705.
- [216] O. Madelung, U. Rössler, in Group IV Elements, IV-IV and III-V Compounds. Part B Electronic, Transport, Optical and Other Properties (Ed: M. Schulz), Springer-Verlag, Berlin 2002.